This is the accepted manuscript of the article: Sun, H., Zhang, L., Wang, Y., Qin, Y., Xie, Z., Ashi, L., Xu, N., Huang, K., Wang, J., & Huang, J. (2025). Improving fatigue life of a titanium alloy through coupled electromagnetic treatments. International Journal of Fatigue, 191, Article 108676. Advance online publication. https://doi.org/10.1016/j.ijfatigue.2024.108676

Improving fatigue life of a Titanium Alloy through coupled electromagnetic treatments

Hongfei Sun [a], Liang Zhang [b], Yuan Wang [a], Yi Qin [c], Zhiqiang Xie [d], Lila Ashi [a], Ning Xu [b], Kunlan Huang [a, *], Jie Wang [a], Jigang Huang [a]

[a] *School of Mechanical Engineering, Sichuan University, Chengdu, Sichuan 610065, P.R. China*

[b] *Harbin Marine Boiler Turbine Research Institute, Harbin, Hei Longjiang 150078, P.R. China*

[c] *Centre for Precision Manufacturing, DMEM, The University of Strathclyde, James Weir Building, 75 Montrose Street, Glasgow G1 1XJ, UK*

[d] *AECC AERO Science and Technology Co., Ltd, Chengdu, Sichuan 610503, P.R. China*

[*] *Corresponding author: E-mail address: huangkunlan@scu.edu.cn (Kunlan Huang)*

Nomenclature	Full name
CEMT	*Coupled Electromagnetic Treatment*
WEDM	*Wire Electrical Discharge Machining*
UT	*Untreated*
AC	*Alternating Current*
DC	*Direct Current*
WD	*Width Direction*
LD	*Length Direction*
σ_{rs}	*Residual Stress before CEMT*
σ'_{rs}	*Residual Stress after CEMT*
SEM	*Scanning Electron Microscope*
EBSD	*Electron Backscattered Diffraction*
TEM	*Transmission Electron Microscope*
KAM	*Kernel Average Misorientation*
LAGB	*Low Angle Grain Boundaries*
HAGB	*High Angle Grain Boundaries*
GND	*Geometrically Necessary Dislocation*
I	*Current Strength*
Cp	*Specific Heat Capacity*
D	*Density*
α_t	*Thermal Expansion Coefficient*
ε	*Strain*
E_t	*Elastic Modulus*
σ	*Stress*
f	*Lorentz force Density*
B	*Magnetic flux Density*
$\Delta\varepsilon$	*Strain Increment*
σ_F	*Stress amplitude*
N_f	*Number of cycles to Failure*
A	*Fatigue strength Coefficient*
b	*Basquin Exponent*
σ_b	*Tensile strength*
δ	*Percentage elongation*

Abstract: TC11 titanium alloy is widely used in the manufacture of key components such as blades of gas turbine and aero engine because of its high specific strength and good processing performance. In the case of gas turbine or aero engine, the fatigue performance of TC11 will directly determine the life of the turbine or engine, and the surface residual stress generated on the alloy during manufacturing often affects the fatigue life of the material. In this study, a new method of coupled electromagnetic treatment (CEMT) was applied to regulate the surface residual stress of the alloy after manufacturing, so as to improve the fatigue life of the TC11. The results show that after the CEMT, the residual compressive stress in the length direction and width direction increased by 63.7% and 56.0% respectively, the fatigue life of the TC11 is increased by 39.9%. The microstructure analysis shows that after CEMT, the width of fatigue striations is significantly reduced. This paper proposes that CEMT can be used as an effective method to adjust the residual stress of materials and improve the fatigue life of titanium alloys. The research is also relevant for improvement of the fatigue life of other alloy materials.

Keywords: Coupled Electromagnetic Treatment; Titanium Alloy; Fatigue Life; Residual Compressive Stress;

1. Introduction

Titanium and titanium alloys have the advantages of being non-magnetic and having low density, high strength, and corrosion resistance, etc. As structural materials, they are widely used in aerospace products, ships, vehicles, the chemical industry, biomedicine and other fields [1-3]. For key components such as compressor disks and blades of aero-engines, good fatigue performance is an important goal. Because these key components work under the combined action of centrifugal force, thermal stress and air excitation force, high frequency resonance and flutter will occur. These complex and harsh working conditions bring great challenges to the fatigue life of materials [4-12]. Study has shown that the residual stress can significantly influence fatigue resistance of engineering components [13-17]. The impact of residual stress is dependent on the state of the residual stress, the existence of the residual compressive stress field can offset the tensile stress in the partial alternating stress and reduce the loading tensile stress [18, 19]. Therefore, how to adjust the residual stress on the surface of the material to improve the fatigue life has become the focus of research.

Residual stress during the machining process is mainly caused by non-uniform plastic deformation, which will store a large amount of elastic strain energy in the workpiece [20]. The principle of improving the residual stress is to adjust it by inputting external energy to the surface or subsurface of the material. The microplastic deformation caused by the external energy causes a change of the elastic strain energy stored in the material during the processing. At present, three methods exist for the removal of residual stress, namely, heat treatment method, mechanical treatment and external field treatment method. Heat treatment methods such as induction hardening [21] and thermal-cooling cycling cause different orientations of grains and sediments to undergo different degrees of thermal expansion and cold contraction through transition from high to low temperatures. The local expansion and contraction will cause micro-stress, and the magnitude and direction of this micro-stress will affect the residual stress [22]. Mechanical methods such as shot peening induces[23-25] local plastic deformation on the surface by hitting the material surface with hard spherical shots, a plastically-stretched surface attempts to expand, but the adjacent elastic region restrains the expansion, creating a compressive residual stress field near the surface. However, this method of improving residual stress by mechanical stress will increase the possibility of surface or subsurface crack initiation, which will

limit the fatigue properties of the material[18, 25].

To solve the above problems, a method for residual stress regulation by generating pulsed current and magnetic fields using a simple device is proposed, this is an external field treatment method. It is often used in metallurgy and metal modification treatment, and has attracted widespread attention due to its rapid, low-temperature, and environmentally friendly characteristics. Zhong et al. [26] found that the electromagnetic coupling treatment could significantly reduce the residual stress of a P10 tool. Cai and Huang et al. [27] found that magnetic field can promote dislocation depinning, and the transmitted electron energy provided by pulsed current can accelerate dislocation motion which leads to the alleviation of residual stress. Ashi et al. [28] found that the electromagnetic coupling treatment can promote internal uniform micro-plastic strain, and produce a maximum of 90×10^3 Pa stress, which provides the power for the dislocation motion and eventually leads to stress relief. Zeng et al.[29] found that CEMT can promote residual stress relaxation of 2A02 aluminum alloy blades, and the effect of CEMT is better than that of single electric or magnetic field treatment, which can reduce the overall stress level of blades by 53%. Zeng et al.[30] found that CEMT could induce current and magnetic fields in CEMT samples, and plastic strain accumulates by simulation. Li et al.[31] found that the effect of the CEMT on the fatigue performance of the treated welds is more significant, comparing to the untreated weld samples, the fatigue limit of the treated samples had an increase of 10.4 %.

This paper aims to improve the amplitude and uniformity of residual compressive stress of a TC11 titanium alloy by CEMT, and to improve the ability of TC11 titanium alloy to resist cyclic loads, thus improving the fatigue life. The results show that CMET can effectively improve the amplitude and uniformity of residual stress, by comparing the fatigue life and residual stress of materials before and after CMET, the optimal specimen number to balance the improvement of fatigue life and the preservation of mechanical properties was established. The mechanism of improving the amplitude and uniformity of residual compressive stress was determined by observing the dislocation morphology combined with the simulation analysis of the electromagnetic field, from this the reason for the improvement of material fatigue life is revealed. This paper provides a reference value for the effective application of CEMT technology in the fatigue life improve of metallic materials.

2. Materials and experimental methods

2.1 Materials

The experimental materials of this study are taken from TC11 sheet material, as shown in Fig. 1a; the sheet thickness is 3 mm, and the chemical composition of the alloy is shown in Table 1. The bulk sample is processed by wire electrical discharge machining (WEDM), as shown in Fig. 1b, and these were sampled by WEDM to 20mm × 10mm × 2mm, shown in Fig. 1e, and used for microstructure observation. Meanwhile, tensile specimens based on the International Standard (ISO 6892-1:2019) were sampled from the block sample for the tensile test; as shown in Fig. 1c. Fatigue and residual stress test specimens based on the Air Standard (HB 5277-1984) were sampled from the block sample, as shown in Fig. 1d. The thickness of tensile sample and fatigue sample is 2mm, the specific size is shown in the Fig. 1c and Fig. 1d.

Table1 TC11 titanium alloy standard composition

Composition	Ti	Al	Mo	Zr	Si	Fe	C	Other
Wt.%	80.042	6.763	3.064	1.412	0.265	0.210	0.082	Bal

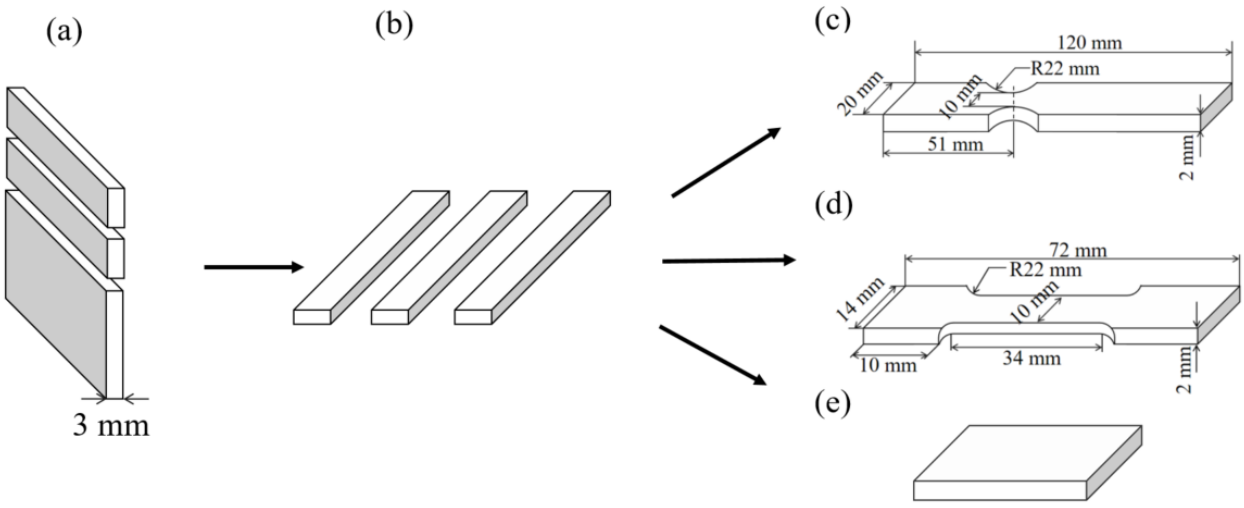

Fig. 1. Schematic diagram of sampling (a) Raw material (b) Block sample (c) Tensile specimens (d) Fatigue and Residual stress test specimens (e)Microstructure characterization specimens

2.2 Coupled electromagnetic treatment experiments (CEMT)

The CEMT experiments shown in Fig. 2a were completed by the CEMT experimental platform designed and customized by Sichuan University (Chengdu, China), The experimental platform

includes a control driving part and a working part. The control drive part is composed of the test bench, cylinder and guide rail. The copper electrode is controlled horizontally on the guide rail through the air pressure transmission and the clamping function of the treated sample is realized. The working part is composed of a magnetic field generating device, a closed electric field loop forming device and two pulse power supply devices.

Fig. 2b shows the CEMT process of specimen. After the copper electrode is driven by the cylinder to clamp the TC11 titanium alloy material, the electric field pulse power supply device, the copper electrode and the sample form a closed loop to make the pulse current pass through. The pulsed electric field is shown in Fig. 2c. At the same time, the magnetic field pulse power supply device and the magnetic field coil form a closed loop. The induced magnetic field is shown in Fig. 2d. By controlling the synchronous control of the pulse power supply, the electromagnetic field can be generated and ended at the same time, and the CEMT of the sample can be realized.

The processing parameters of electromagnetic coupling significantly influence the properties of TC11 titanium alloy. Previous studies primarily concentrated on the voltage as a key electric field parameter across various metal materials[32-34]. However, for workpieces composed of different materials and possessing distinct geometric dimensions, identical voltage levels can yield varying current values. Consequently, the process parameter for the electric field in electromagnetic coupling treatment is defined as current density (A/mm²). Song et al.[35] conducted electrical pulse treatments on TC11 titanium alloy at a current density of 56.2 A/mm², revealing that while the fatigue performance of TC11 titanium alloy improved to some extent, residual compressive stress gradually diminished with increasing treatment duration. At elevated current densities such as 100 A/mm² [36], significant phase transitions occurred in TC11 titanium alloys alongside improvements in their fatigue life. Song et al.[37] emphasized that to achieve optimal results from electromagnetic treatment, magnetic flux density should not fall below 1 T. Therefore, based on the aforementioned research findings, this study establishes a current density gradient ranging from 40 A/mm² to a maximum of 200 A/mm² and sets the magnetic flux density gradient between 0.5 T and up to 1.5 T. The formulated process parameters according to orthogonal experimental design principles are presented in Table 2.

Table 2 CEMT processing parameters

Treatment	Specimen number								
	#0	#1	#2	#3	#4	#5	#6	#7	#8
Magnetic field intensity (T)	0	1.5	1.5	1.5	1.5	1.5	0.5	1.0	2.0
Electric field intensity (A/mm^2)	0	40	80	120	160	200	120	120	120

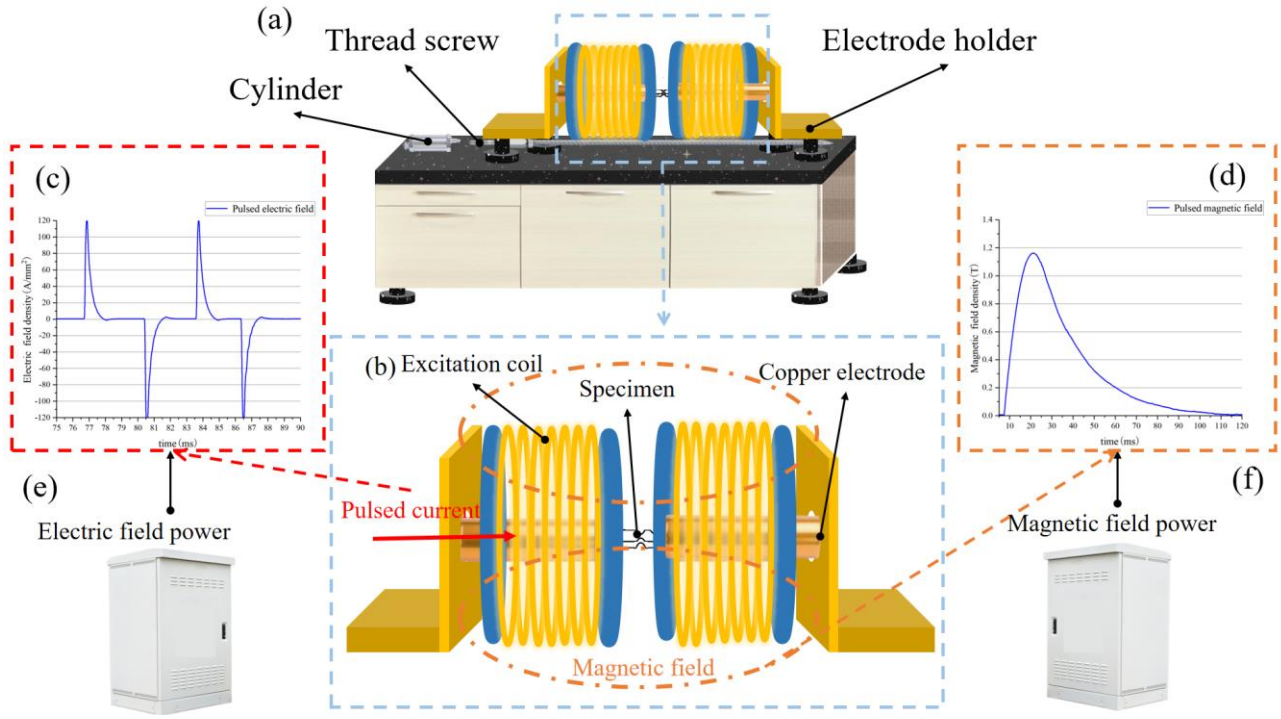

Fig. 2. (a) Schematic of CEMT experimental platform; (b) electromagnetic field generation; (c) pulse AC sawtooth wave current; (d) magnetic field intensity at the central symmetry of the coil axis, (e) Pulsed electric field generating device, and (f) pulsed magnetic field generating device

2.3 Experimental measurements

As shown in Fig. 3, the surface residual stress of the specimens in both the width direction (WD) and length direction (LD) was measured by the X-ray diffraction method (Proto LXRD 1200W) before and after CEMT. Cu Kα radiation was used as the X-ray source with a beam area of Φ2 mm. The diffraction crystal face was <213>. The residual stress analysis was performed by the sin2ψ technique. Eight tilt angles (ψ) were applied, and 15 exposures with a duration of 1 s were carried out at each position. The macro residual stress was estimated from the measurements of X-ray diffraction peaks fitted by the Gaussian distribution function. The residual stress test points are shown in Fig. 3. Five points are selected in the variable cross-section area of the specimen. Among them, point 1, point 2

and point 3 measure the longitudinal residual stress in the width direction, and point 2, point 4 and point 5 measure the transverse residual stress in the length direction.

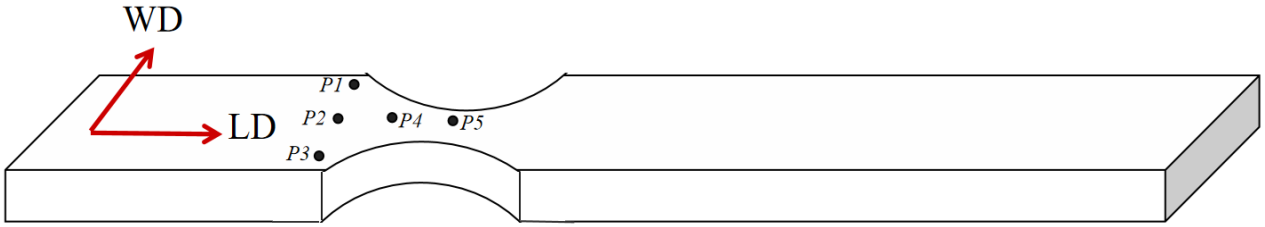

Fig. 3. Residual stress test points.

The tensile properties were tested by a ETM305D microcomputer controlled electronic universal testing machine. For each specimen number, three tensile specimens were used to measure the tensile strength, and the mean value was used as the tensile strength of the specimen number. Accordingly, three tensile specimens without CEMT were tested as the control group.The mechanical properties of TC11 titanium alloy are shown in Table 3.

The fatigue test was carried out by a WDW-RD100 metal material creep rupture tester. All fatigue samples were polished to the mirror state (Ra = 0.8) to eliminate the influence of surface roughness on fatigue performance. The fatigue test parameters were loaded peak F = 13kN, loaded frequency f = 10Hz, stress ratio R = 0.1, and the load form was sine wave. Three samples were selected for fatigue test under the electromagnetic coupling process parameters. The average number of fatigue cycles at fracture was taken as the fatigue performance of the TC11 titanium alloy under this process parameter.

2.4 Microstructure observation

The microstructure was characterized by a quasi-in-situ experiment designed by scanning electron microscope (SEM). After cutting, grinding and polishing, the observation surface was chemically corroded by Kroll reagent (5% HF + 15% HNO_3 + 80% H_2O), and the observation area was characterized by micro-indentation for the first time. After that, the sample block was subjected to the CEMT, and the position was calibrated by micro-indentation and the second SEM characterization was carried out.

The phase content, phase boundary angle and local misorientation angle of the TC11 titanium alloy before and after CEMT were further characterized by electron backscatter diffraction (EBSD). The specific experimental steps were as follows: (1) The observation surface of the sample was selected, and the electrolytic polishing was carried out at room temperature for 2 minutes by polishing solution

($HClO_4$:CH_4O = 1:9). The acquisition step was set to 0.25μm, and the scanning resolution was 260 × 260. The scanning area of 65 × 65 μm^2 was scanned by EBSD, and the position of the scanning area was calibrated and the data were recorded with micro-indentation. (2) CEMT of the sample; (3) Locate the scanning area by micro-indentation, perform EBSD scanning again, and record the data; (4) The experimental data were analyzed by HKL CHANNEL5 software.

The precipitated phase and dislocation dynamic behavior (such as dislocation tangles and dislocation twins) of the TC11 titanium alloy before and after CEMT were observed by transmission electron microscopy (TEM). After wire cutting and mechanical polishing, the samples before and after CEMT were prepared by an ion beam thinning instrument (Gatan 695). TEM uses FEI Talos F200X G2 (FEI), which has a 200 kV acceleration voltage and a maximum resolution of 0.12 nm. The phase composition is crystallography-calibrated by selecting electron diffraction at the phase boundary and at a specific position. At the same time, the atomic arrangement is observed by high-resolution transmission at the interface of dislocation motion and precipitated phase.

2.5 Numerical simulation

The CEMT of TC11 titanium alloy material involves the coupling effect of multi-physical fields such as electric field, magnetic field, temperature field and structural mechanics field simultaneously. These four fields can be solved simultaneously by COMSOL Multiphysics software. The geometric model of CEMT of the sample is constructed by three-dimensional modeling software, as shown in Fig. 4. The electrodes, coils and TC11 titanium alloy samples are placed in a specific analysis domain (ideally air). The two electrodes are in direct contact with the sample, and the sample is placed at the center of the two electrodes. The coil is simplified into a specific shape by using a multi-turn coil, which can save the amount of computation and operation time while ensuring the accuracy of the calculation results. The numerical simulation performance parameters are shown in Table 4, and the finite element meshing is shown in Fig. 4.a. Fig.4.b shows the meshing and meshing quality of the whole electromagnetic coupling processing geometric model. Fig. 4.d shows the meshing of TC11 titanium alloy samples. As the main object of attention in the electromagnetic coupling process, the mesh is divided into regular hexahedrons according to the geometry of the sample with the side length is less than 1 mm. The grid division of the electrode, coil and analysis domain is to minimize the amount of computation which still meeting the accuracy requirements of the solution.

Table 3 Parameters of TC11 titanium alloy

Variable	Attribute Name	Unit	Value
ρ_m	Density	g/cm^3	4.48
ρ	Resistivity	$\Omega \cdot m$	1.71×10^{-6}
α	Resistivity temperature coefficient	K^{-1}	1.75×10^{-9}
Cp	Specific heat capacity	J/ (Kg · K)	605
λ	Thermal conductivity	W/ (m · K)	7.5
E	Young's modulus	G Pa	123
ν	Poisson's ratio	-	0.33
σ_b	Tensile strength	MPa	1100
δ	Percentage elongation	%	10

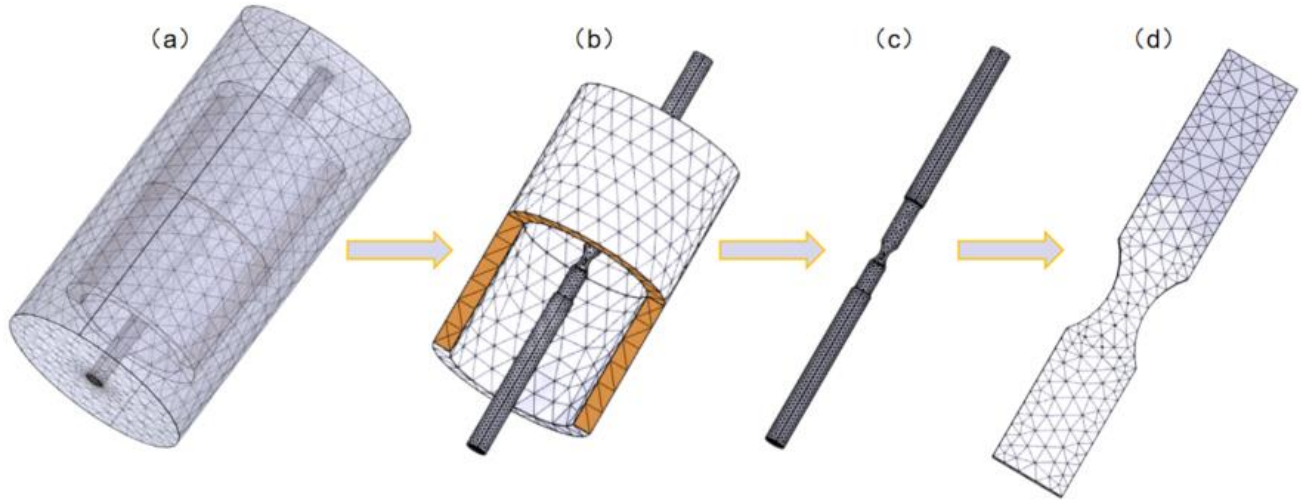

Fig.4 Meshing of CEMT geometric models: (a) whole area; (b)magnetic coil; (c) electrodes and specimens; and (d) tc11 titanium alloy fatigue test specimen

2.6 Estimation method of crack growth rate

The calculation formula of fatigue striation width d is shown in formula (1), where *D* is the width from the first fatigue striation to the nth fatigue striation. The width of fatigue striation is measured many times in each group of morphologies and the average value is taken to reduce the calculation error, which is used to characterize the crack propagation rate. The relationship between fatigue striation and fatigue crack growth rate is shown in Eq. (2)[38]. ΔK is the stress intensity factor range; y is the geometric correction factor; $\Delta\delta$ is the stress range in the cyclic process; a is the width of fatigue striation. Under the same stress load, the wider the fatigue striation, the greater stress intensity range,

the faster the crack growth rate of the material, and the lower the fatigue life of the sample.

$$d = D/(n-1) \tag{1}$$

$$\Delta K = Y\Delta\delta\sqrt{\prod_{1}^{n} a_i} \tag{2}$$

2.7 Calculation method of dislocation density

Studies have shown that KAM can be used to qualitatively characterize changes in the true dislocation density [39]. To explore the relationship between the generation of plastic strain and dislocation movement, the following formulas are used to calculate the geometrically necessary dislocation (GND) density in the specimens:

$$\rho_{GND} = 2\theta / \mu b \tag{3}$$

where ρ_{GND} represents geometrically necessary dislocation density, θ is the mean value of the kernel averaged misorientation in the selected area, μ is the scanning step size, b is the Burgers vector. The parameter θ can be expressed as:

$$\theta = \exp\left[\frac{1}{N}\sum_{1}^{i} \ln KAM_{L,i}\right] \tag{4}$$

where $KAM_{L,i}$ is the KAM value at point i, and N is the number of points in the test area.

3. Experimental results

3.1 Residual stress

The increase of residual stress in the length direction of the TC11 titanium alloy by CEMT with different process parameters is between 5.9 % and 63.7 %, as shown in Fig.5. The sign + / - denotes the type of residual stress (residual tensile stress / residual compressive stress). Table4 shows the increased amplitude and increased rate of residual stress of TC11 titanium alloy fatigue specimens under different process parameters. By comparing the process parameters # 1 ~ # 5, the influence of current density increasing from 40A/mm^2 to 200A/mm^2 on the residual stress of TC11 titanium alloy fatigue specimen under the same magnetic field condition (magnetic flux density is 1.5T) can be explored. Except for the current density of 80A / mm^2, the effect of residual stress increase is not significant, the increase rate is 5.9 %, and the increase of residual stress under other current densities is between 53.4 % and 63.7 %. In the case of current density of 120A / mm^2 and 200A / mm^2 (# 3 and

5), the residual stress increase rate is higher, the increase rate is 63.7 % and 57.2 % respectively. In the case of current density of 40A / mm^2 and 120A / mm^2 (# 1 and # 3), the residual stress increase amplitude is higher, the increased amplitude is 50.4Mpa and 67.5Mpa respectively. Therefore, Considering the increased amplitude and rate, it is preliminarily determined that 120A / mm^2 (#3) is the better process parameter to improve the residual stress of TC11 titanium alloy. By comparing the process parameters # 6, # 7, # 3 and # 8, the regulation effect of the increase of magnetic flux density on residual stress under the same electric field condition (current density of 120A / mm^2) can be explored. When the magnetic flux density is 0.5T, 1.0T, 1.5T and 2.0T, the residual stress increase rates of TC11 titanium alloy fatigue specimens are 6.1 %, 57.8 %, 63.7 % and 19.0 %, respectively. The improvement effect shows a trend of increasing first and then decreasing. When the magnetic flux density is 1.5T, the residual stress increase rate is the highest, so it can be initially used as a better parameter to improve the residual stress of TC11 titanium alloy material.

Table 4 The change of residual stress in the LD under different process parameters

Specimen number	σ_{rs} (MPa)	σ'_{rs} (MPa)	Increase amplitude (MPa) $\sigma'_{rs}-\sigma_{rs}$	Increase rate (%) $(\sigma'_{rs}-\sigma_{rs})\ /\sigma_{rs}$
#1	-114.7	-165.1	-50.4	44.0
#2	-112.3	-118.9	-6.6	5.9
#3	-105.9	-173.4	-67.5	63.7
#4	-71.2	-109.2	-38.0	53.4
#5	-55.3	-87.0	-31.7	57.2
#6	-163.3	-173.3	-10.0	6.1
#7	-113.4	-179.0	-65.6	57.8
#8	-135.1	-160.8	-25.7	19.0

The average residual stress in the width direction of TC11 titanium alloy material before and after CEMT under different process parameters is shown in Fig. 6. Table 5 shows the increased amplitude and increased rate of residual stress of TC11 titanium alloy fatigue specimens under different process parameters. By comparing the process parameters # 1- # 5, it can be found that with the increase of current density, the residual stress increase effect is more significant under the conditions of 120A/mm^2

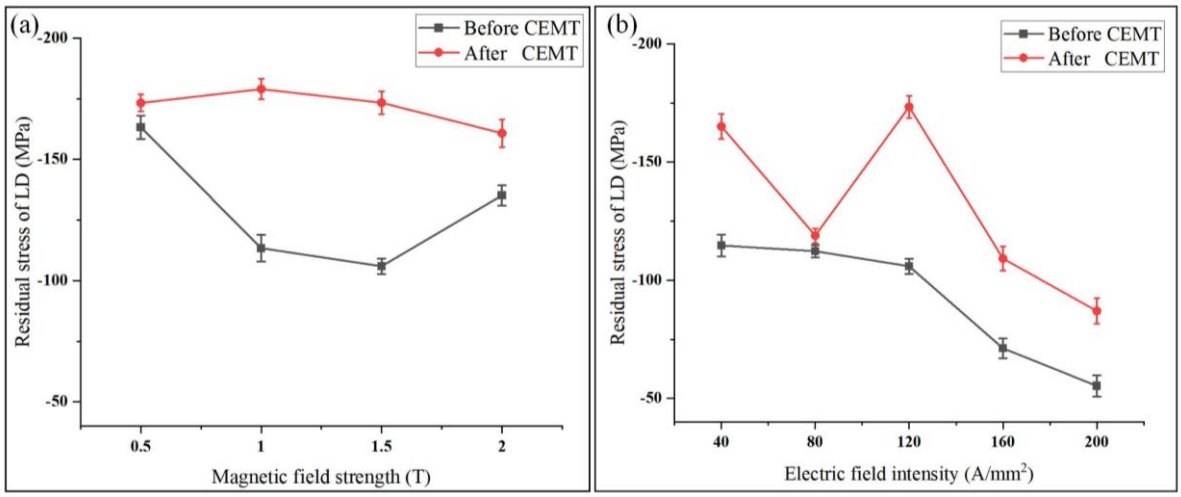

Fig.5 (a) Effect of magnetic field intensity on residual stress in LD direction (b) Effect of current density on residual stress in LD direction

and 200A/mm^2, and the increase rates are 56.0 % and 45.2 %, respectively, while the change of residual stress under other electric field parameters is small. Therefore, it is preliminarily considered that the above two electric field parameters are the better process parameters to control the residual stress in the width direction of the TC11 titanium alloy fatigue specimen. At the same time, comparing the process parameters # 6, # 7, # 3 and # 8, it is found that the residual stress increases by 7.2% when the magnetic flux density is 1.0T, and the effect is not significant. At 0.5T, 1.0T and 2.0T, the residual stress increases by 66.4%, 56.0% and 117.4% respectively. It can be preliminarily considered that the residual stress in the width direction of the TC11 titanium alloy fatigue specimen is the best when the magnetic flux density is 2.0T.

Table 5 The change of residual stress in WD under different process parameters

Specimen number	σ_{rs} (MPa)	σ'_{rs} (MPa)	Increase amplitude (MPa) $\sigma'_{rs}-\sigma_{rs}$	Increase rate (%) $(\sigma'_{rs}-\sigma_{rs})\ /\sigma_{rs}$
#1	-150.1	-139.6	10.5	-7.0
#2	-135.2	-163.7	-28.5	21.1
#3	-101.5	-158.3	-56.8	56.0
#4	-137.2	-145.6	-8.4	6.1
#5	-112.4	-163.2	-50.8	45.2
#6	-115.9	-192.8	-76.9	66.4
#7	-150.2	-161	-10.8	7.2
#8	-70.1	-152.4	-82.3	117.4

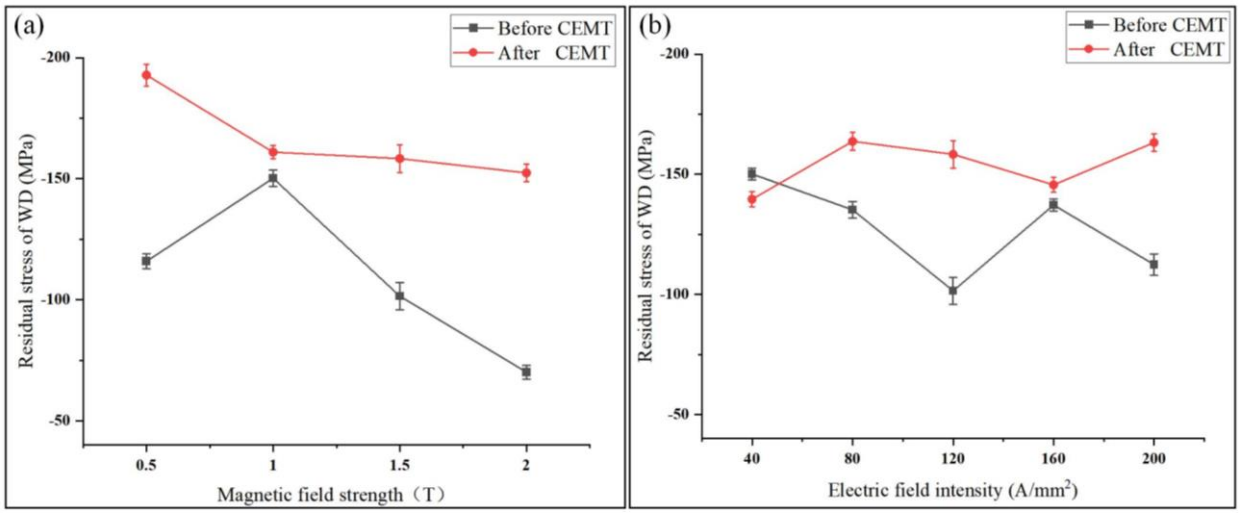

Fig.6 (a) Effect of magnetic field intensity on residual stress in WD direction (b) Effect of current density on residual stress in WD direction

3.2 Fatigue life and mechanical properties

Three replicates were selected for fatigue tests for each specimen number, while specimen #0 acted as the control group. The fatigue life of the TC11 titanium alloy fatigue specimens under different CEMT parameters is shown in Fig.7. Under most of the CEMT process parameters, the fatigue life of the fatigue specimen is significantly improved, and the fatigue life of the TC11 titanium alloy fatigue specimen is increased by 3.7 % ~ 39.9 %. The fatigue performance of the material is the most significant under the process parameter # 3 (1.5T, 120A / mm^2). By comparing the process parameters # 1- # 5 to explore the effect of current density change on the improvement of material fatigue performance, it is found that the higher current density has a better effect on the improvement of fatigue life of titanium alloy. By comparing the process parameters # 6, # 7, # 3 and # 8, it is found that the fatigue performance of TC11 titanium alloy is significantly improved under higher magnetic flux density.

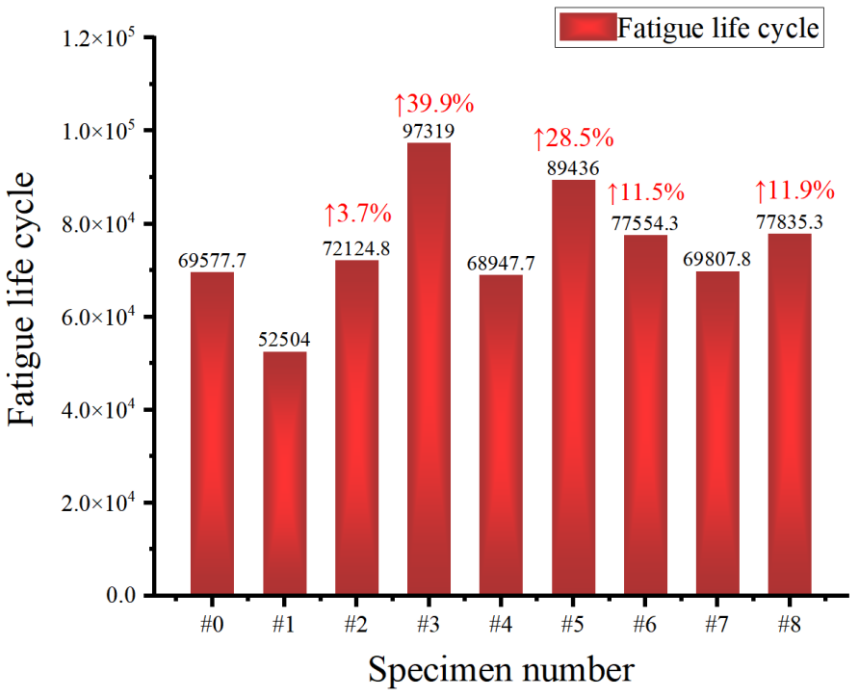

Fig.7 The fatigue cycles of TC11 titanium alloy under different process parameters

Three replicates were selected for tensile tests for each specimen number, while specimen #0 acted as the control group. The tensile strength and its error bar were shown in Fig.8(a). After electromagnetic treatment, the tensile strength of TC11 titanium alloy tensile samples remained basically unchanged. The tensile strength of # 1, # 3, # 4, # 5, # 7 and # 8 samples increased to varying degrees. Among them, the # 1 sample increased the most, the tensile strength increased by 9.26 MPa, and the increase was 0.84 %. The tensile strength of # 2 and # 6 samples decreased, and the # 6 sample decreased the most. The tensile strength decreased by 2.14 MPa, and the decrease was 0.19 %. The overall data showed that the electromagnetic treatment did not affect the tensile strength of TC11, that is, the strength remained unchanged. As shown in Fig.8 (b), the elongation of TC11 titanium alloy tensile samples before and after electromagnetic treatment has different degrees of improvement. Among them, the elongation of # 3 sample increased by 11.4 %, and the other samples increased by 1.3 % (# 6) ~ 9.5 % (# 1). The overall data show that electromagnetic treatment can improve the elongation of TC11 titanium alloy material, that is, improve the plasticity of the material. The above data show that the electromagnetic treatment technology can effectively improve the plasticity of the material without affecting the strength of the material.

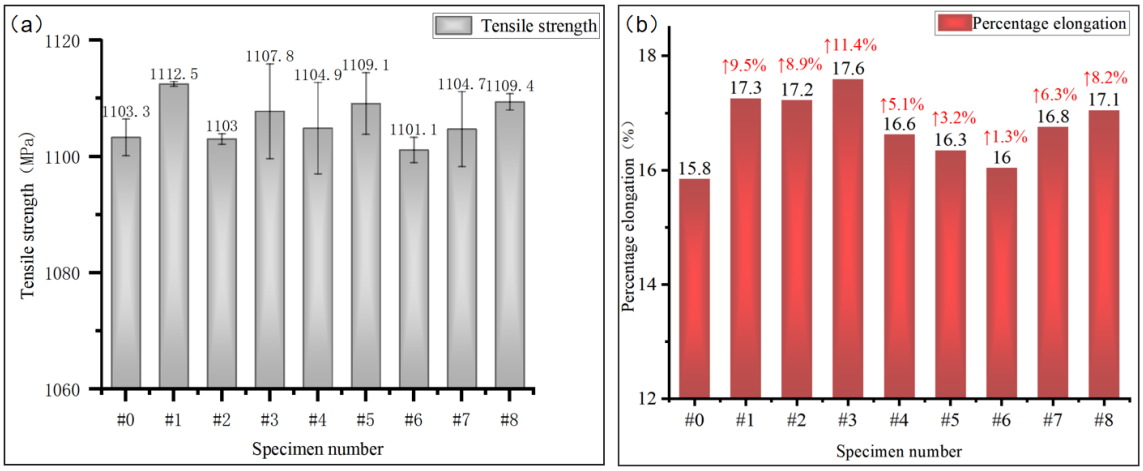

Fig.8 Comparison of (a) tensile strength, and (b) percentage elongation before and after CEMT

3.3 Microstructure observation

3.3.1 SEM observation of fatigue crack source

The fatigue source area morphology of the TC11 titanium alloy fatigue specimens under different CEMT process parameters is shown in Fig. 9[35, 40]. The fatigue source of the specimen without the CEMT is located on the surface of the specimen (Fig. 9a). The cracks caused by multiple sources extend and converge to the interior of the material with the stress cycle, and finally form a ' fatigue step ' area with high stress concentration inside the specimen and brittle fracture occurs. Under the process parameter # 1, the fatigue crack source of the material migrates from the surface layer to the subsurface layer (Fig. 9b), and the fatigue crack moves radially in the subsurface layer. It is worth noting that under the process parameter #1, the residual compressive stress decreases in the width direction of the sample, which also explains that the fatigue life of the material under the process parameter # 1 is significantly lower than that of the untreated group. Under the process parameter # 2 (Fig. 9c), the fatigue crack source of the material further moves to the middle of the sample, and the fatigue crack propagation form presents a common beach pattern, that is, the fatigue crack propagation path moves to the surface layer perpendicular to the direction of the wavy pattern. Under this process parameter, there is no obvious step-like crack morphology caused by stress concentration at the defect. Therefore, the fatigue fracture is mainly affected by the residual compressive stress, and the crack initiates from the middle of the sample to the surface, thereby improving the fatigue life of the material. By analyzing the fatigue crack propagation form of the material under the process parameter # 3 (Fig. 9d), it is found that the crack source is located on the surface of the material similar to the untreated

group, but the crack source size is significantly reduced and the distribution is dispersed. The fatigue cracks initiated from the two crack sources expand radially in different directions of the material, and there is no merger of crack sources. Therefore, there is no obvious cleavage step caused by stress concentration on the fracture surface. Therefore, it can be considered that under this set of process parameters, the internal stress concentration during the fatigue experiment is alleviated, so the fatigue performance of the material under this set of process parameters is the best. Similarly, the analysis of Fig. 9e-i shows that the fatigue crack sources of the material after CEMT are distributed in the subsurface or inside of the sample, which beneficially hinders the speed of crack initiation and expansion under periodic load environment and improve the fatigue life of the material. With the continuous loading of alternating load, the crack propagation path shows common beach-like patterns and shell-like patterns (Cowrie Pattern). In the process of crack propagation, the stress concentration caused by crack aggregation will cause the fracture to show cleavage steps, which will damage the fatigue life of the material. This also explains the different fatigue life of materials under different CEMT process parameters.

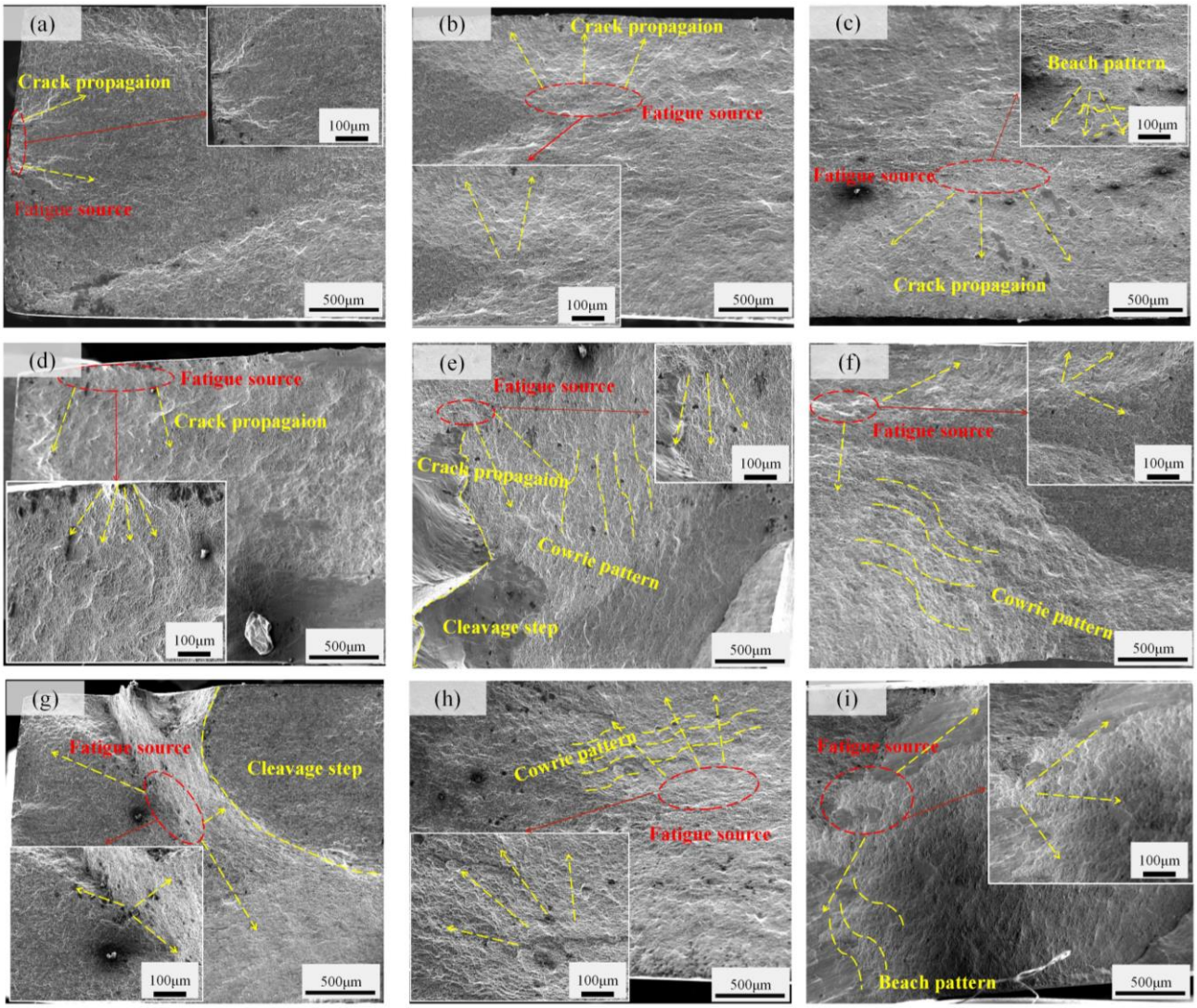

Fig. 9 The morphology of titanium alloy fatigue source area under different CEMT process parameters: (a) - (i): Process parameters # 0- # 8

3.3.2 SEM observation of fatigue crack growth

After the fatigue crack initiation, the crack will slowly expand along the direction perpendicular to the load under the action of tensile stress. At this time, the fatigue specimen changes from the plane stress state to the plane strain state, and obvious plastic strain begins to appear inside the material characterized by a large number of parallel fatigue striations. Fatigue striation is the trace left by discontinuous propagation along the front of a fatigue crack. Each boundary is the advancing position of the crack under a certain stress cycle. By analyzing the typical morphology of the fatigue fracture crack propagation zone, the fatigue crack propagation speed and propagation behavior of the titanium alloy after CEMT can be characterized. The morphology of the fatigue crack propagation zone under

different electromagnetic coupling process parameters is shown in Fig.10. The red arrow in the Fig. is Crack Propagation Direction; the green arrow represents the secondary crack morphology; the strip-like morphology perpendicular to the direction of crack propagation is fatigue striation, which is represented by yellow parallel line segments.

The fatigue striation width of the untreated group was 0.817μm, while in Section 4.1, the fatigue striation widths of several groups of process parameters # 1, # 4 and # 7 (Fig.10(b-3), (e-3) and (h-3))[35, 36] with decreased fatigue life were 0.716μm, 0.723μm and 0.855μm.Therefore, it can be considered that these groups of samples have similar or more than the crack growth rate of the untreated group, so the macroscopic performance is that the fatigue life value is similar to or significantly lower than that of the untreated group. The small secondary cracks in the crack propagation zone indicate that a certain degree of plastic strain is generated in the region, and the main crack tip is bifurcated. The emergence of secondary cracks will release the local concentrated residual stress and produce local stress relaxation, thus effectively hindering crack propagation[39]. This also explains why the fatigue striation width of the sample under the process parameter # 2 is higher than that of the untreated group, and the fatigue crack propagation speed becomes faster, but the fatigue life still exceeds the untreated group. As shown in Fig. 10(c-3), there are more secondary cracks in the direction of fatigue crack propagation, the stress field is relaxed at the secondary crack area, and the stress range $\Delta\ \delta$ is reduced. Finally, Finally, the stress intensity factor range $\Delta\ K$ is reduced. The material needs to undergo more cyclic loads, and the fatigue crack will continue to expand under higher tensile stress accumulation. It is worth noting that the morphology of Fig. 10(d-3) also explains the reason why the material has the highest fatigue life value under the process parameter # 3: multiple short secondary cracks are dispersed on the crack propagation path, which indicates that a certain degree of plastic deformation occurs in the matrix during the fatigue fracture process. The crack is hindered by the secondary crack during the propagation process, so the rate and efficiency is reduced. Therefore, the macroscopic performance is that the fatigue life of the material is most significantly improved.

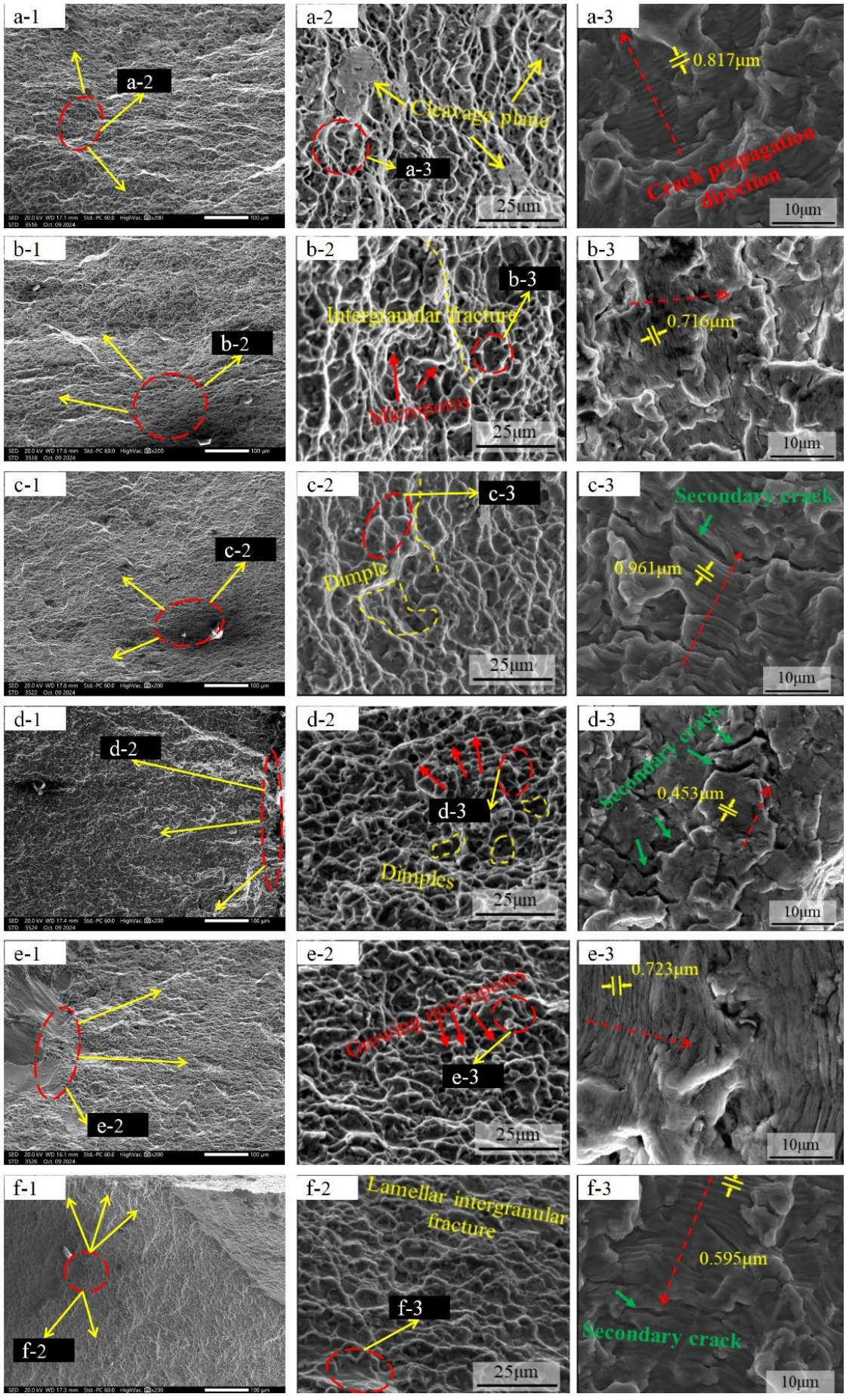
a-1
a-2
a-2
Cleavage plane
a-3
25μm
a-3
0.817μm
Crack propagation direction
10μm
b-1
b-2
b-2
b-3
Intergranular fracture
Microvoids
25μm
b-3
0.716μm
10μm
c-1
c-2
c-2
c-3
Dimple
25μm
c-3
Secondary crack
0.961μm
10μm
d-1
d-2
d-2
d-3
Dimples
25μm
d-3
Secondary crack
0.453μm
10μm
e-1
e-2
e-2
Growing microvoids
e-3
25μm
e-3
0.723μm
10μm
f-1
f-2
f-2
Lamellar intergranular fracture
f-3
25μm
f-3
0.595μm
Secondary crack
10μm

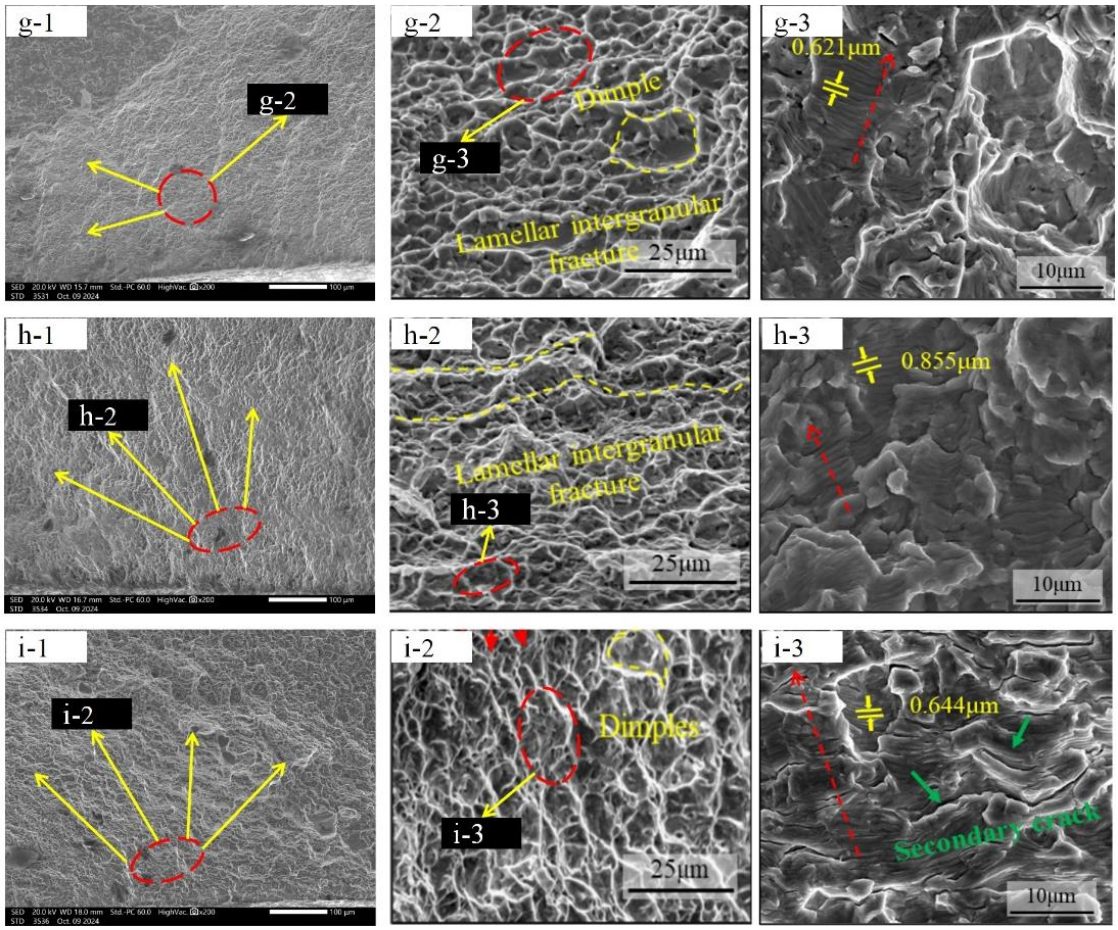

Fig.10 Morphology of fatigue source region of titanium alloy under different CEMT process parameters: (a) - (i): process parameters # 0- # 8

3.3.3 SEM observation of phase composition

According to Section 3.1 and 3.2, the effects of residual stress and fatigue life improvement are the best for specimen number #3 (120A/mm^2, 1.5T). The optimal specimen number (120A/mm^2, 1.5T) is selected for subsequent microstructure observation.

Fig.11[35, 41, 42] shows the SEM image of the initial microstructure of TC11 titanium alloy. It is composed of primary α phase (gray part), β phase (red frame bright part) and secondary acicular α phase (acicular phase), and presents the morphology of α + β equiaxed structure [43]. The α phase has a close-packed hexagonal structure (HCP). The matrix is mainly composed of Ti, Al and Zr elements, and the average grain size is 10 μm. The β phase is a body-centered cubic (BCC) structure, which is mainly composed of Ti, Mo and Si elements, and the average grain size is 2.5 μm.

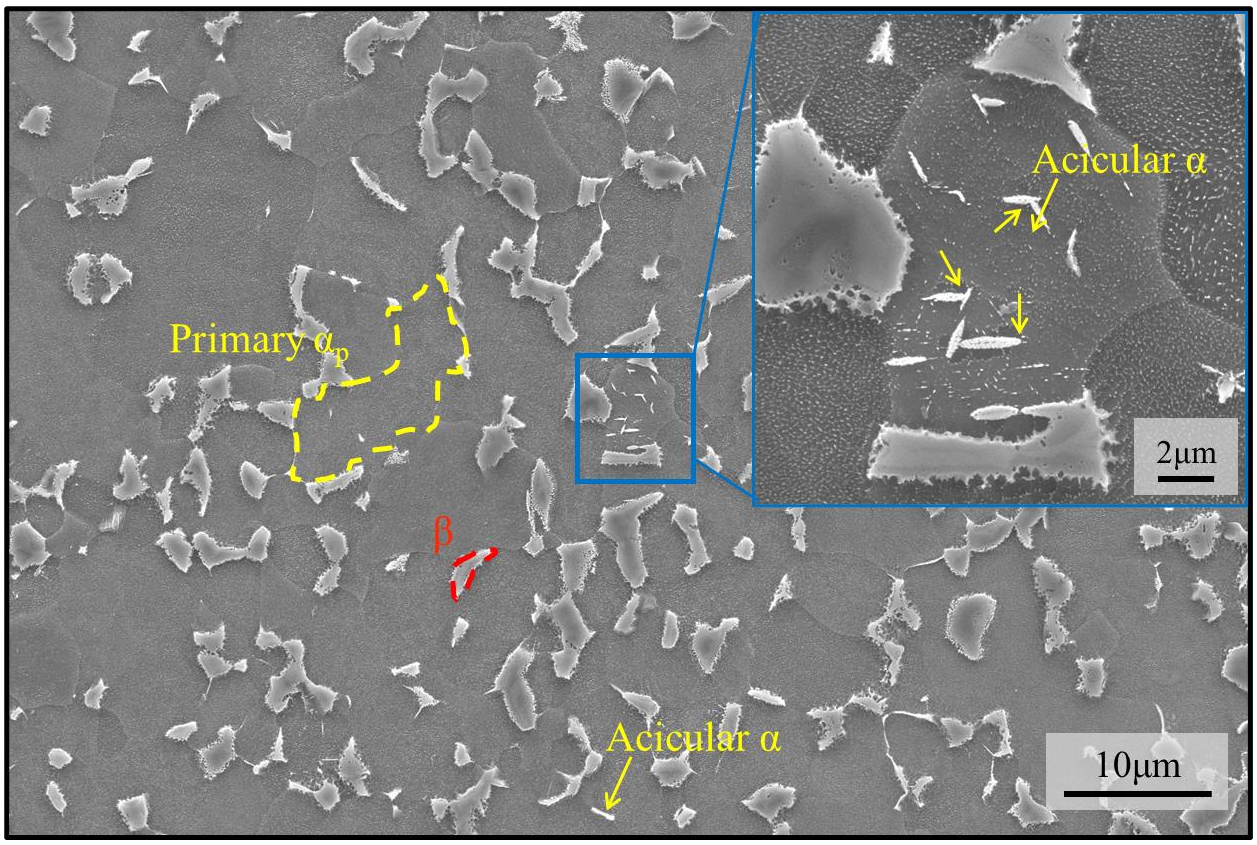

Fig. 11.SEM image of the initial microstructure morphology of TC11 titanium alloy.

In order to explore the influence of CEMT technology on the distribution and content of two phases, the three field of view regions of TC11 titanium alloy before and after CEMT were observed by the SEM characterization method, and the results were shown in Fig. 12[35, 41, 42]. Similar to the initial microstructure morphology, the CEMT did not significantly change the phase distribution morphology of TC11 titanium alloy. It was still dominated by the dispersed β phase in the α matrix, showing equiaxed distribution characteristics, and a small amount of needle-like secondary α phase was dispersed at the junction, which had a certain degree of dispersion strengthening effect.

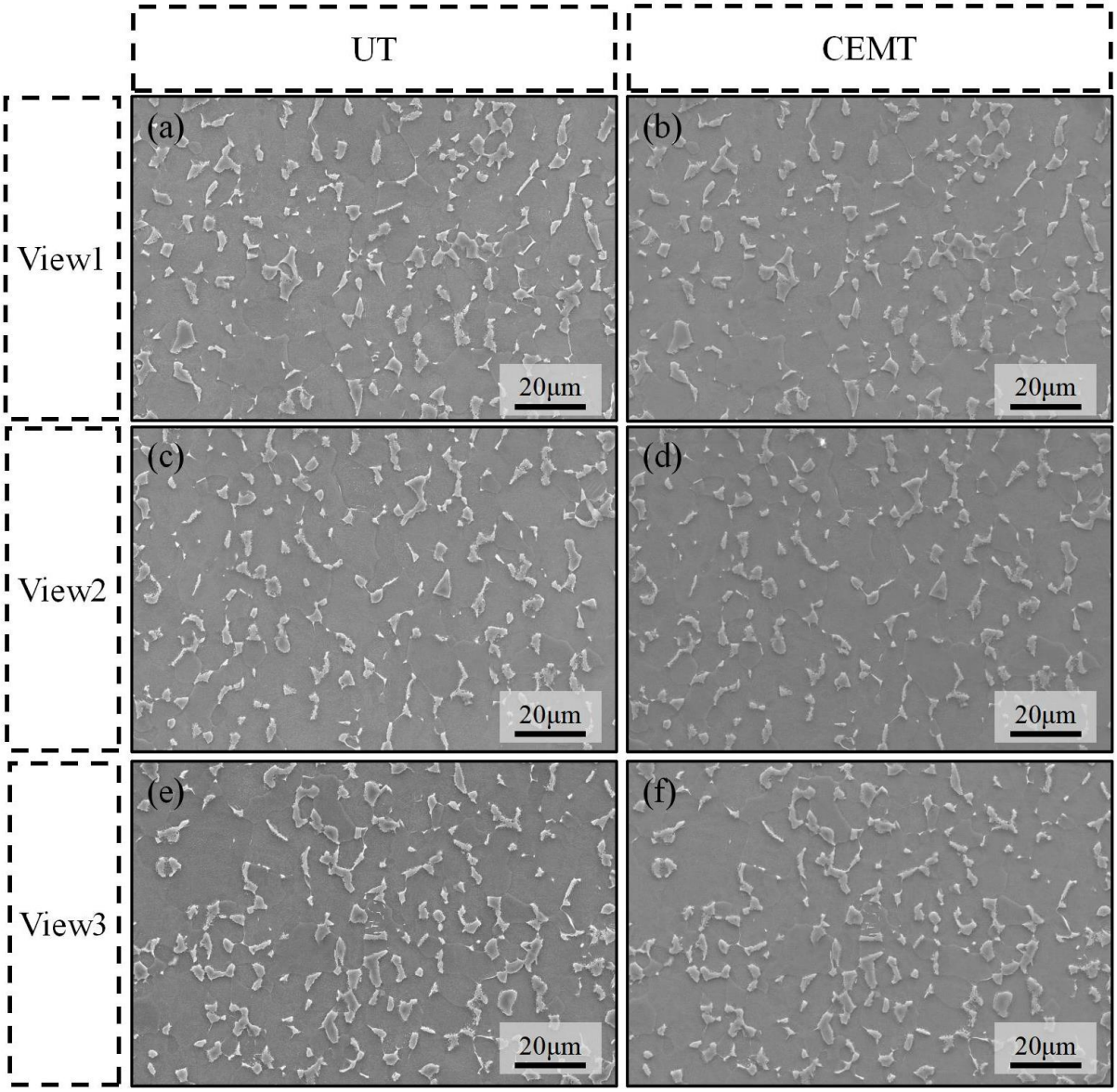

Fig 12 Microstructure morphology of TC11 titanium alloy: (a), (c) and (e) UT;(b), (d) and (f) CEMT

In order to further explore the influence of CEMT on phase composition, Image-Pro Plus software was used to process the collected image data, and the area ratio of the two phases was statistically analyzed. The results are shown in Table 6. After CEMT, the area ratio of α phase is slightly increased, the area ratio of β phase is slightly decreased, and the results are consistent in three fields of view. Under the condition of ignoring statistical error, it can be preliminarily considered that TC11 titanium alloy does not undergo obvious phase transformation under the optimal process parameter # 3.

Table 6The proportion of two phases before and after CEMT in different fields of view

View	UT		CEMT	
	α phase	B phase	α phase	β phase
View1	91.53%	8.47%	91.64%	8.36%
View2	87.97%	12.03%	88.16%	11.84%
View3	86.24%	13.76%	86.34%	13.66%
Average	88.58%	11.42%	88.71%	11.29%

3.3.4 EBSD observation

A Euler diagram of titanium alloy samples before and after CEMT is shown in Fig. 13, in which the color of different grains represents different orientation angles. Similar to the observation at the SEM scale, the crystal structure of the material is composed of equiaxed α + β Comparing Fig. 13a and b, it can be found that some smaller-sized grains undergo a turning behavior after CEMT, such as the grains in Fig. 13a and b. Further, Fig.13c shows the orientation relationship of the grains at four positions in the field of view before and after the CEMT (black is untreated, red is after CEMT). It is found that the Euler angles (*Φ1*, *Φ2* and *Φ3*) along the *X*, *Y* and *Z* directions have changed significantly, that is, the orientation of the grains has changed significantly. Therefore, it can be considered that the external stress applied by the electromagnetic field provides energy for the preferred orientation of the grains during the CEMT so that the grains are obviously twisted compared with the observation plane.

The grain boundary angle changes within the TC11 titanium alloy samples before and after CEMT were further explored, as shown in Fig. 14. The red line represents the grain boundary with an angle of 0 ~ 15°, that is, the low angle grain boundary (LAGB), and the black line represents the grain boundary with an angle of more than 15°, that is, the high angle grain boundary (HAGB). It can be seen from the diagram that there is no significant difference in HAGB in the material after CEMT, while the content of LAGB increases, which is manifested in the proliferation of LAGB (such as the blue arrow in the diagram) and the diffusion of LAGB into the grain interior (such as the blue circle in the diagram). Fig.14c shows the proportion of grain boundaries with different angles. It can be seen that after CEMT, the proportion of grain boundaries with an internal angle of less than 5° increases significantly.

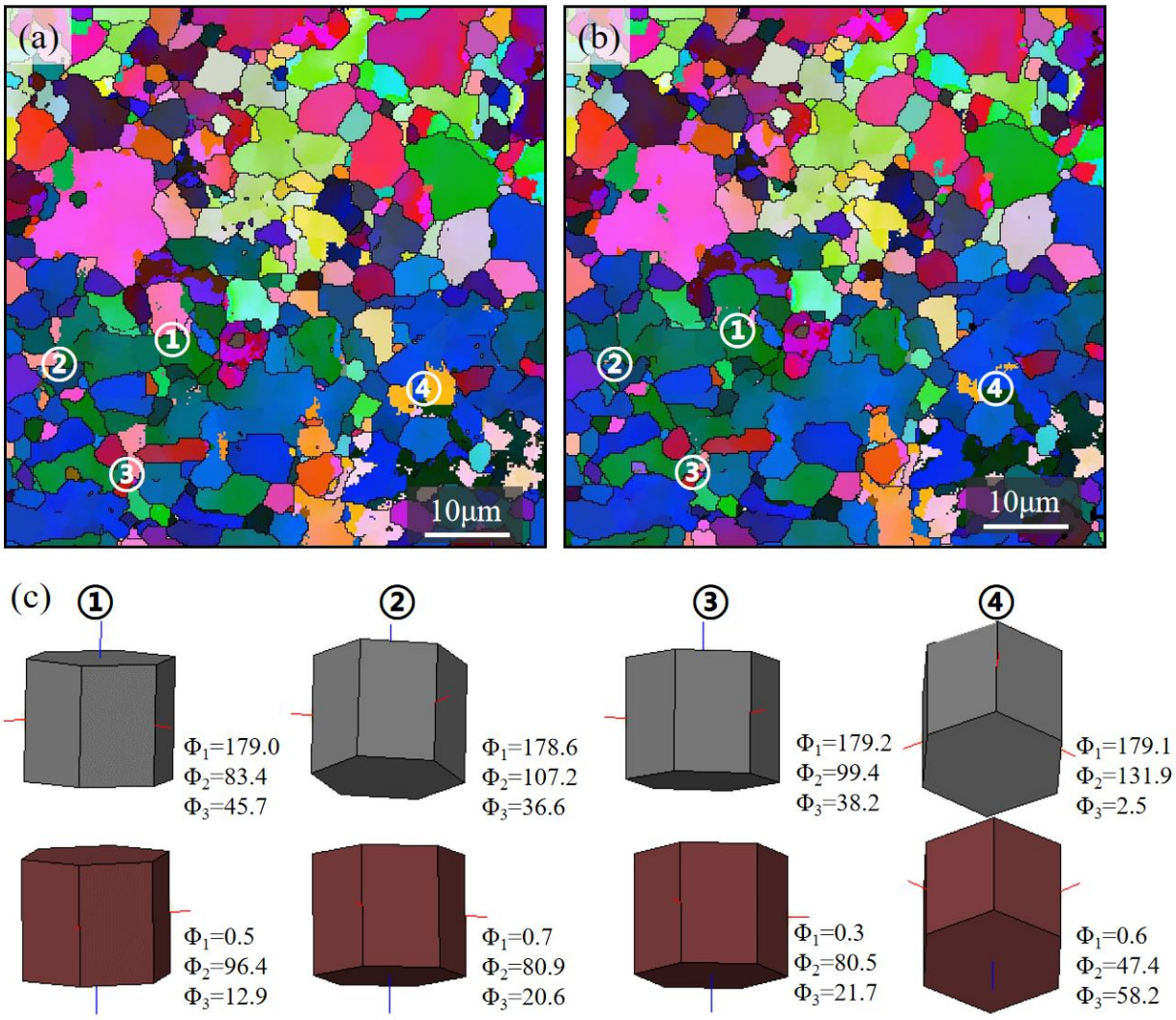

Fig.13 Grain orientation characteristics before and after CEMT: (a) untreated; (b) after CEMT; (c) local grain orientation angle

Due to the different orientation of the grains, the atomic arrangement in the two adjacent grains shows different directions and converges to form grain boundaries, so the atomic arrangement at the grain boundaries is in an irregular high-energy state. The relationship between grain boundary energy and grain orientation angle can be expressed as Eq. 3

$$\gamma = \gamma_0 \theta / (A - \ln \theta) \tag{5}$$

where γ is the grain boundary energy, θ is the grain boundary angle, A is an integral constant, and γ_0 is a constant, which is only related to the material.

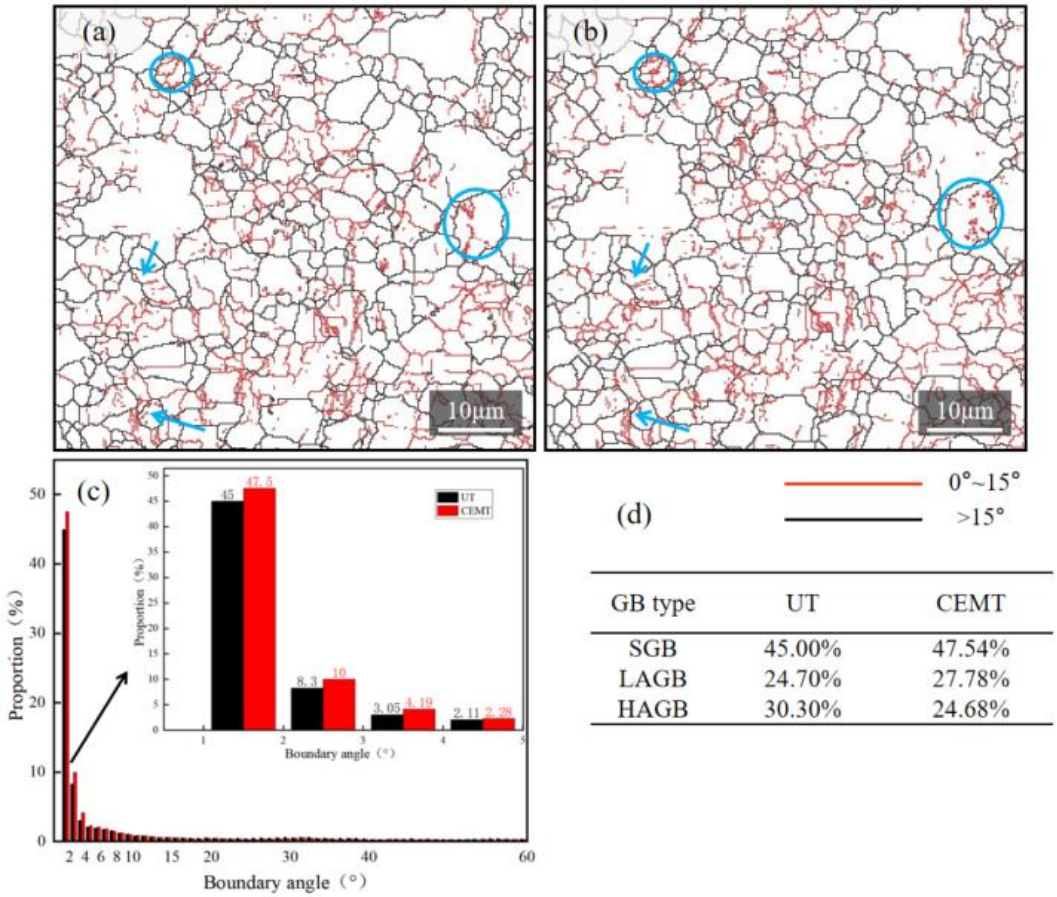

GB type	UT	CEMT
SGB	45.00%	47.54%
LAGB	24.70%	27.78%
HAGB	30.30%	24.68%

Fig.14 Changes of grain boundary angle before and after CEMT: (a) UT; (b) CEMT; (c) grain boundary angle statistical diagram; (d) statistical table of grain boundary angle content

It can be seen from formula 3 that HAGB has high grain boundary energy and usually becomes a channel for stress corrosion and crack propagation. LAGB has lower grain boundary energy, resistivity and diffusion coefficient, which can inhibit intergranular corrosion and crack propagation. The increase of low-angle grain boundaries will significantly hinder the movement of material dislocations and resist the expansion of cracks. The statistics of different grain boundary contents before and after CEMT are shown in Fig.14d. The increase of SGB and LAGB contents increased from 45.00 % and 24.70 % to 47.54 % and 27.78 %, respectively. This indicates that significant dislocation slip occurs in the sample during the CEMT, and due to the high-energy obstacles of the irregular arrangement of atoms at the high-angle grain boundaries, dislocations tend to slip into the interior of the grains, eventually forming sub-grain boundaries (SGB), thereby improving the fatigue life of the sample.

The Kernel Average Misorientation (KAM) of the TC11 titanium alloy before and after CEMT was analyzed by EBSD, as shown in Fig. 15. The greener the color, the higher the local misorientation angle value. The value of local misorientation angle is often used to characterize the degree of plastic

deformation in the material [44]. Comparing Figs.15a and b, it can be found that the initial plastic strain area of the sample is concentrated at the large angle grain boundary (black solid line), and there is also a small strength plastic strain area in some larger grains. After CEMT, the concentration of the plastic strain region is effectively improved, the green part gradually slips into the grain, and the overall plastic strain shows a uniform dispersion distribution trend, which is consistent with the change of the small angle grain boundary. Fig. 15c shows the fitting curve of the distribution of the local misorientation angle before and after CEMT. After CEMT, the peak value of the curve decreases and the overall right shift, indicating that the overall misorientation angle of the sample shows an increasing trend.

In this study, the scanning step of EBSD is 0.5 μm, and the Burgers vector of TC11 titanium alloy is 0.361nm. The mean value of KAM and geometric dislocation density of TC11 titanium alloy before and after CEMT are shown in Fig.15d. After CEMT, the density of GND increases from 16.512×10^{15} m^{-2} to 18.905×10^{15} m^{-2}, about 14.5%, which quantitatively explains the rightward shift of the curve in Fig. 15c.

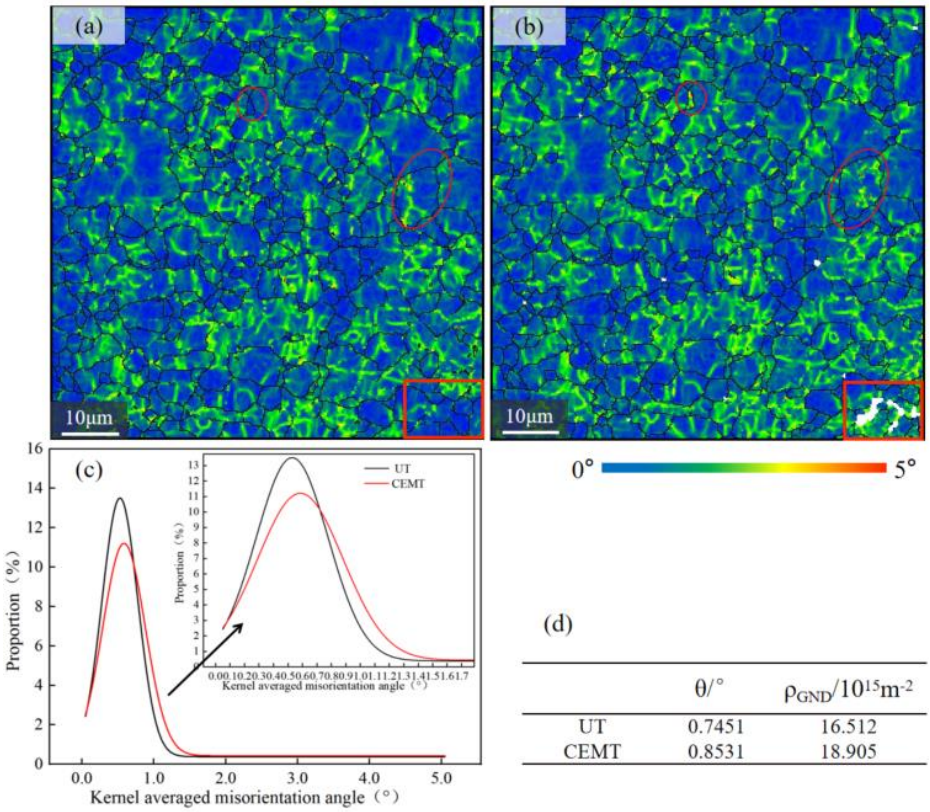

	θ/°	$\rho_{GND}/10^{15}m^{-2}$
UT	0.7451	16.512
CEMT	0.8531	18.905

Fig. 15. KAM map of TC11 titanium alloy: (a) UT; (b) CEMT; (c)distribution curves of KAM density; (d) mean value of KAM and geometric dislocation density of TC11 titanium alloy

3.3.5 TEM observation

The experimental data of EBSD have repeatedly confirmed the phenomenon of dislocation motion during the electromagnetic coupling process. With this phenomenon, the increase of recrystallized grains in the material, the formation of sub-grain boundaries, the uniform distribution of microplastic strains and the increase of geometric dislocation density are produced. Therefore, the untreated and electromagnetic coupling treated TC11 titanium alloy samples were further characterized by TEM to analyze the evolution behavior of dislocations during this process.

The TEM morphology of the untreated and electromagnetically coupled TC11 titanium alloy samples is shown in Fig. 16. The untreated sample shows obvious dislocation pile-up and dislocation entanglement at the grain boundary. The above phenomenon will lead to the concentration of local stress and the strain energy at the grain boundary is too large, this would increase the risk of cracks. After CEMT, the dislocation entanglement at the grain boundary is alleviated, and the dislocation migrates into the grain along the slip system under the action of the electromagnetic field. The obvious dislocation slip phenomenon can be observed from 16 (b), and the dislocation presents a highly parallel state. At the same time, the sub-grains are gradually formed during the dislocation movement, which further confirms the phenomenon that the proportion of sub-grain boundaries in EBSD increases. The dislocation cross-slip process will form an interlaced dislocation network structure. After CEMT, the content of dislocation network decreases, and the dislocations in the grains gradually become edge dislocations.

The dislocation is essentially the lattice distortion in the crystal material, which belongs to a kind of line defect from the geometric point of view. As the carrier of inelastic deformation, the dynamic evolution behavior of dislocation motion, proliferation and annihilation is accompanied by the generation of microplastic strain in the material[45]. Therefore, the dynamic motion behavior of dislocations in TEM images further confirms the reason for the uniform microplastic strain in the EBSD experimental data. Through the movement and proliferation of dislocations, the crack propagation of TC11 titanium alloy material will be more hindered during the fatigue stress cycle, so the fatigue life will be improved.

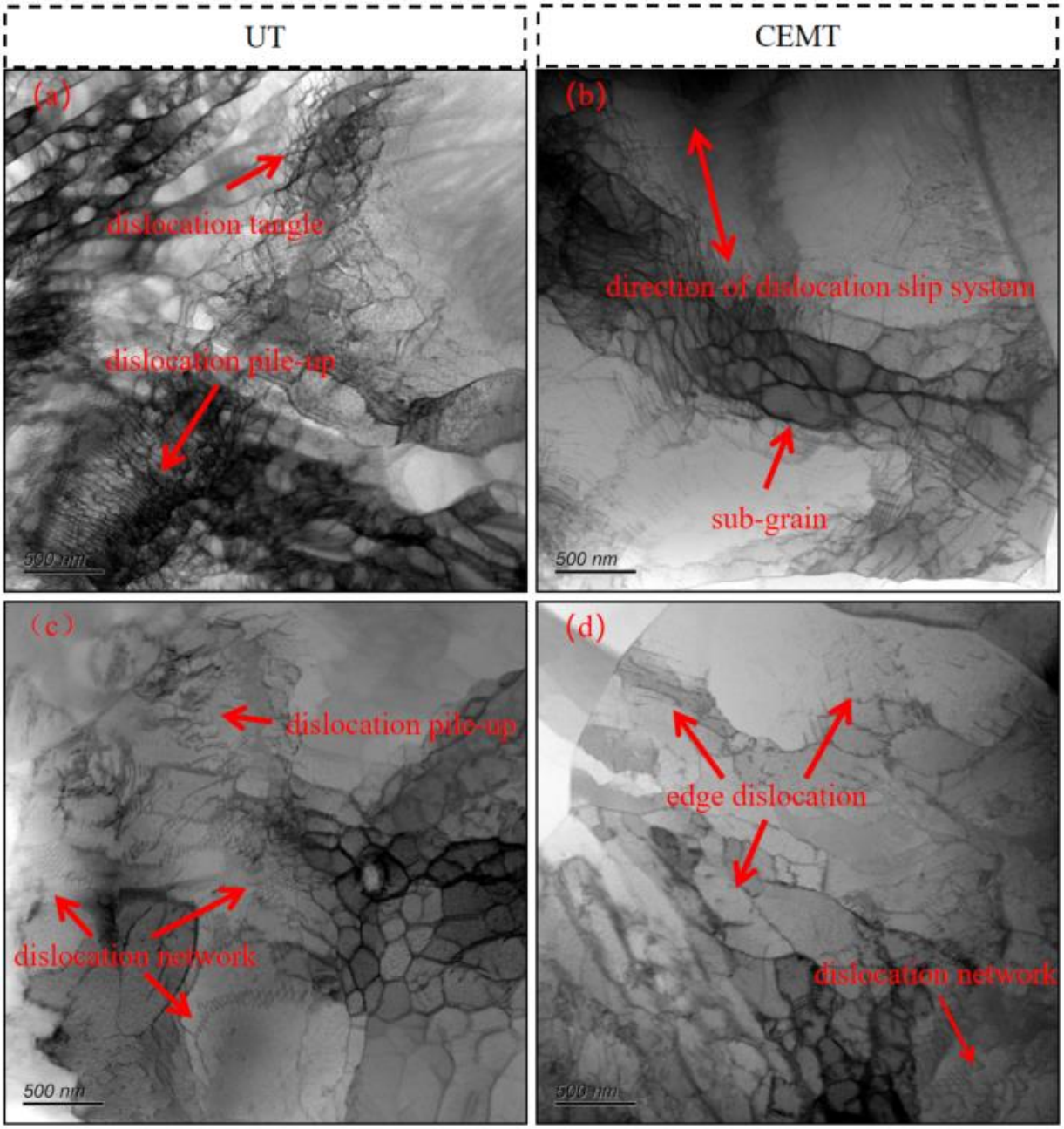

Fig. 16. TEM images of 7050 aluminum alloy specimens: (a), (b) and (c) UT; (d) (e) and (f) CEMT

3.4 Numerical simulation analysis

3.4.1 Electromagnetic field

This section discusses the numerical simulation of the electromagnetic field in the sample based on COMSOL Multiphysics software, including the distribution of current and magnetic fields in the CEMT cycle, as well as the microscopic stress and strain caused by the electromagnetic field and temperature field. Combined with the control results of residual stress and fatigue performance, the #

3 process parameters are selected as the simulation input, and the boundary conditions such as mechanics and heat are added. The coupling analysis of temperature field and stress field is carried out in combination with the electromagnetic field. The output results are shown in Fig.17.In a CEMT processing cycle, including one magnetic pulse and four positive and negative current pulses, t = 1,4 and 10 millisecond are selected for magnetic field and positive current pulse coupling analysis, and t = 12,16 and 20 millisecond are selected for magnetic field and negative current pulse coupling analysis.

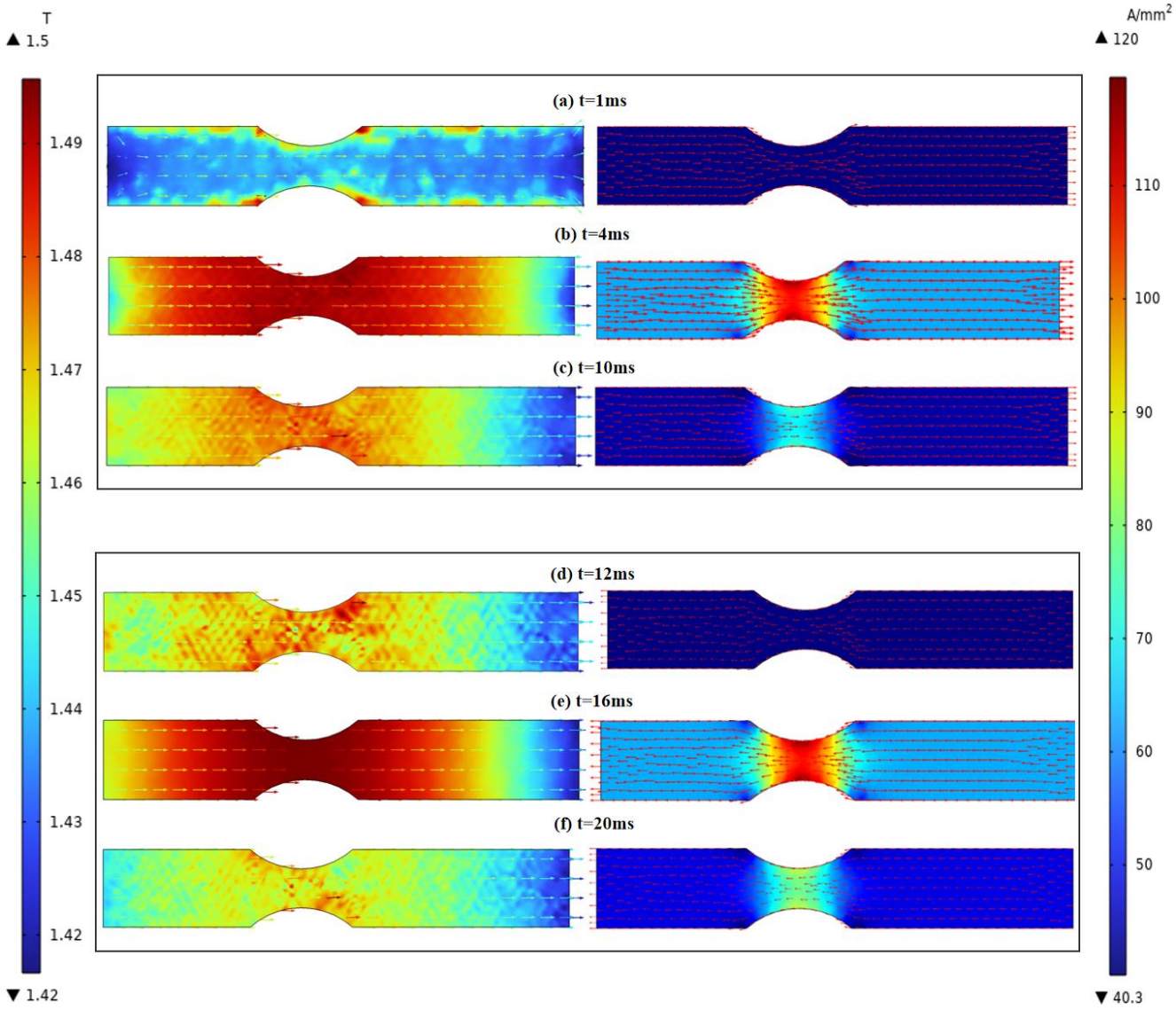

Fig. 17. Intensity and direction of pulsed current (shown on the right) and magnetic field (show on the left), magnetic field and positive current at (a) t=1ms, (b) t=4ms, (c) t=10ms, magnetic field and negative current at (d) t=12ms, (e) t=16ms, (f) t=20ms

The current density distribution at different times of CEMT is shown in Fig.17 (right). Since the input parameter of the simulation process is the current, the current density increases gradually with

the decrease of the cross-sectional area at the variable cross-section. In a period of magnetic field and positive pulsed electric field, the difference of current density distribution is greatly affected by the value of current itself. The current density increases first and then decreases, and it is negatively correlated with the cross-sectional area on the surface of the sample. In a magnetic field and negative pulse electric field cycle, the distribution and change trend of current density is consistent with the positive electric field cycle, only the current direction changes.

Fig. 17 (left) shows the magnetic flux density distribution of the material at different times. Since the variable cross-section area of the material, that is, the gauge area of the fatigue experiment is located at the geometric center of the coil, it can be seen that the magnetic flux density shows a central symmetry characteristic with the gauge area of the TC11 titanium alloy fatigue sample. When t = 4ms and t = 16ms, the pulse magnetic field reaches the peak value, and the magnetic flux density in the gauge region of the material also reaches the peak value of 1.5T. Subsequently, with the attenuation of the input magnetic field, the magnetic flux density in the material gradually decreases, but the decrease is only 5.3 %. Therefore, it can be considered that in an CEMT period, the sample is in a 1.5T magnetic field environment, and the magnetic field treatment effect is significant.

3.4.2 Temperature and thermal stress field

The temperature distribution of the electromagnetic coupling process at different times is shown in Fig.18. The temperature distribution map of the sample was output at a time interval of a current pulse. It can be found that the temperature rise increases with the increase of treatment time.

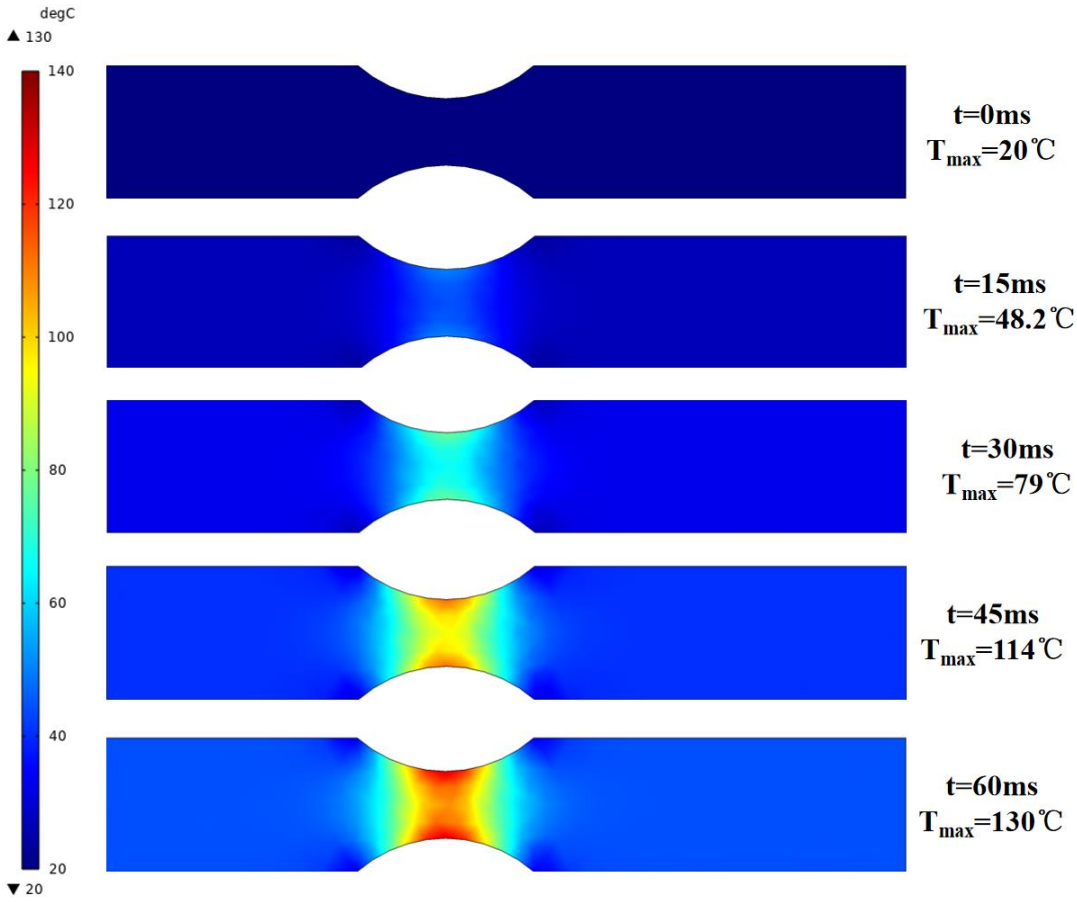

Fig. 18. Electromagnetic coupling processing temperature distribution at different times

Thermal stress is caused by the fixed constraint of thermal expansion caused by temperature change, so it is a process of temperature rise and deformation constraint. For TC11 titanium alloy fatigue specimens, both ends are clamped and fixed during the electromagnetic coupling process, and the temperature difference caused by the change of current density will cause internal deformation constraints. Fig.19 shows the distribution characteristics of mises equivalent stress and volume strain of the material at different times, the stress direction of the specimen surface represents the direction of the maximum principal stress. Similar to the distribution characteristics of current density, when the current density increases rapidly, the thermal stress of the sample also increases rapidly. The peak value is 110 MPa, and the maximum thermal stress occurs at the variable cross section of the sample. The thermal stress range of the sample surface is 40 MPa ~ 110 MPa. The thermal strain is also similar to the distribution characteristics of current density. When the current density increases rapidly, the thermal strain of the sample also increases rapidly, with a peak value of 6.64×10^{3} ppm. The sample expands at the variable cross section, and the thermal strain is positive. The sample is subjected to

compressive stress due to clamping at both ends of the sample, so the strain is negative.

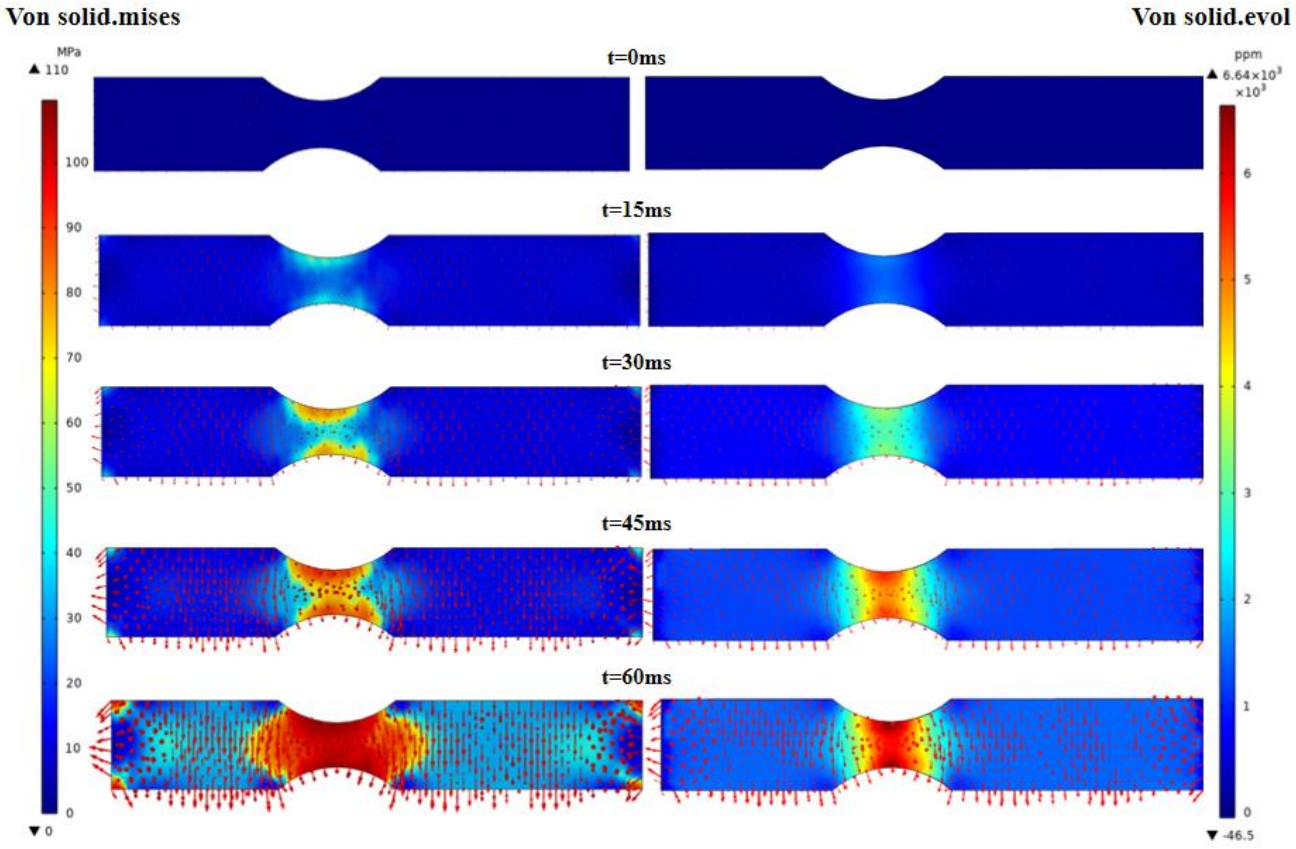

Fig. 19. The stress and strain distribution of CEMT at different times

After CEMT, the temperature change of the sample cooled to the greenhouse after releasing constraint is shown in Fig. 20, and the mises equivalent stress and volume strain change in the corresponding process is shown in Fig. 21, the stress direction of the specimen surface represents the direction of the maximum principal stress. It can be found that after the sample is cooled to room temperature, there are still some residual stresses and strains on the surface of the sample, which are mainly concentrated in the variable cross-section area of the sample, and the residual stresses range from 10 MPa to 40 MPa. The introduced strains ranged from 660 to 1140 ppm.

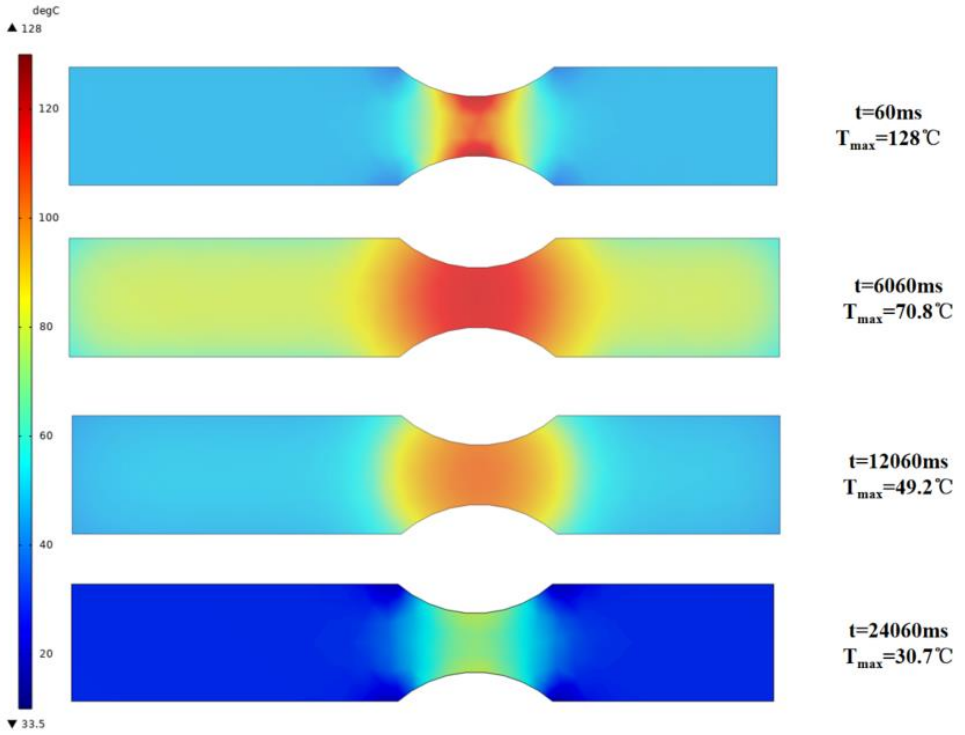

Fig. 20. Temperature change during cooling

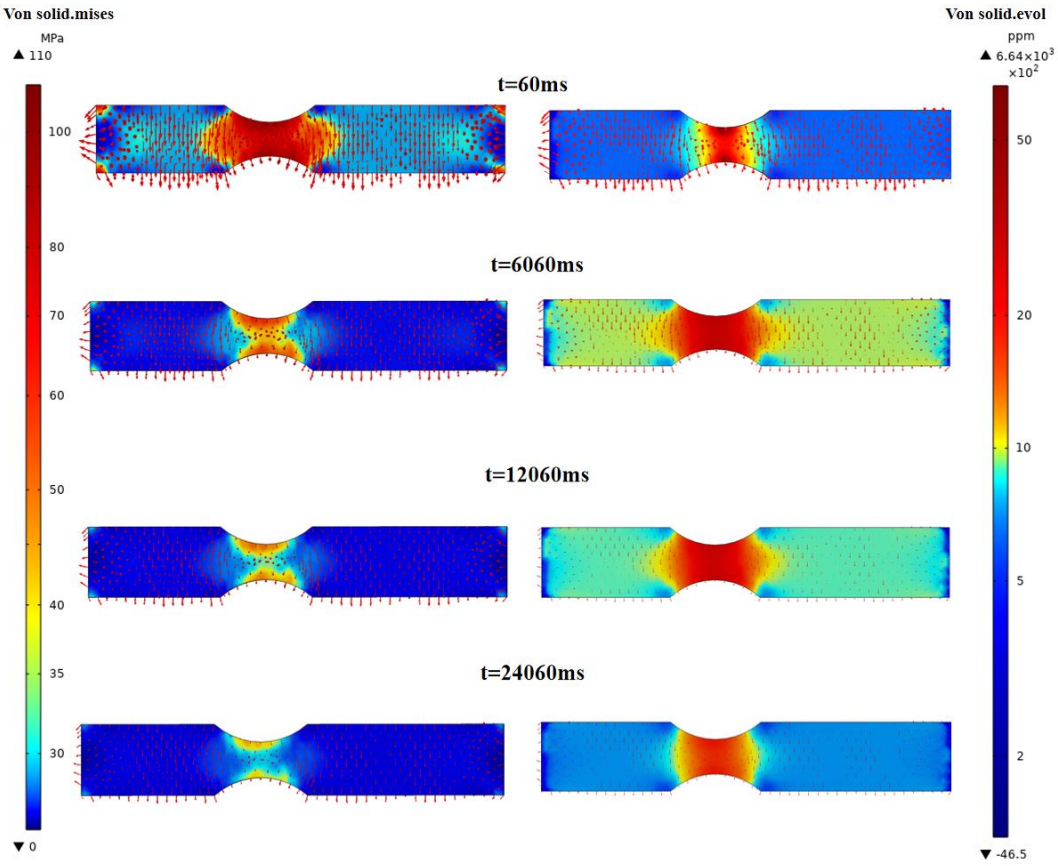

Fig. 21. Stress-strain changes during cooling

3.4.3 Lorentz force

After analyzing the influence of thermal effects in the process of electromagnetic coupling, the influence of non-thermal effects is further discussed. The main manifestation of the non-thermal effect in this process is the Lorentz force. The distribution of the Lorentz force in a single pulsed electric field cycle is shown in Fig.22. It can be found that the Lorentz force is only determined by the current density and the angle between the electric field and the magnetic field. The current direction and the magnetic field direction in the fixed cross-section area of the sample are parallel as shown in Fig17, and there is no Lorentz force. In the variable cross-section area, there is an angle between the current direction and the magnetic field direction as shown in Fig17 that resulting in Lorentz force.

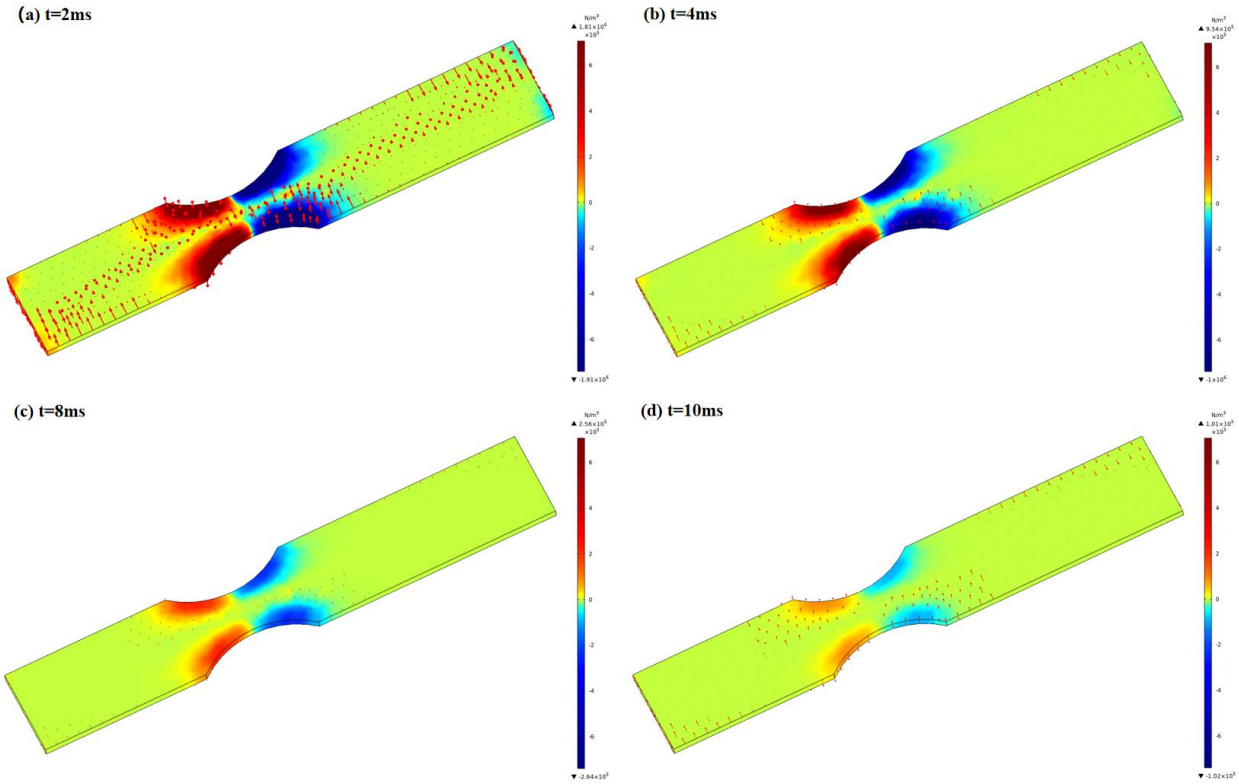

Fig. 22. Lorentz force distribution in a single pulse electric field period

The distribution of Lorentz force in a single CEMT cycle is shown in Fig. 23. The single CEMT cycle is coupled by two groups of positive and negative pulse currents and a single pulse magnetic field. Fig. 23a and 23c represent the distribution of Lorentz force on the surface of the sample under positive pulse current. Fig. 23b and 23d represent the distribution of Lorentz force on the surface of the sample under negative pulse current. It can be found that the Lorentz force is the same at the same

peak current density, but the direction of the Lorentz force in the same region oscillates periodically in a single CEMT cycle. Combined with Fig. 22, it can be found that in a single CEMT cycle, the magnitude and direction of the Lorentz force changes periodically.

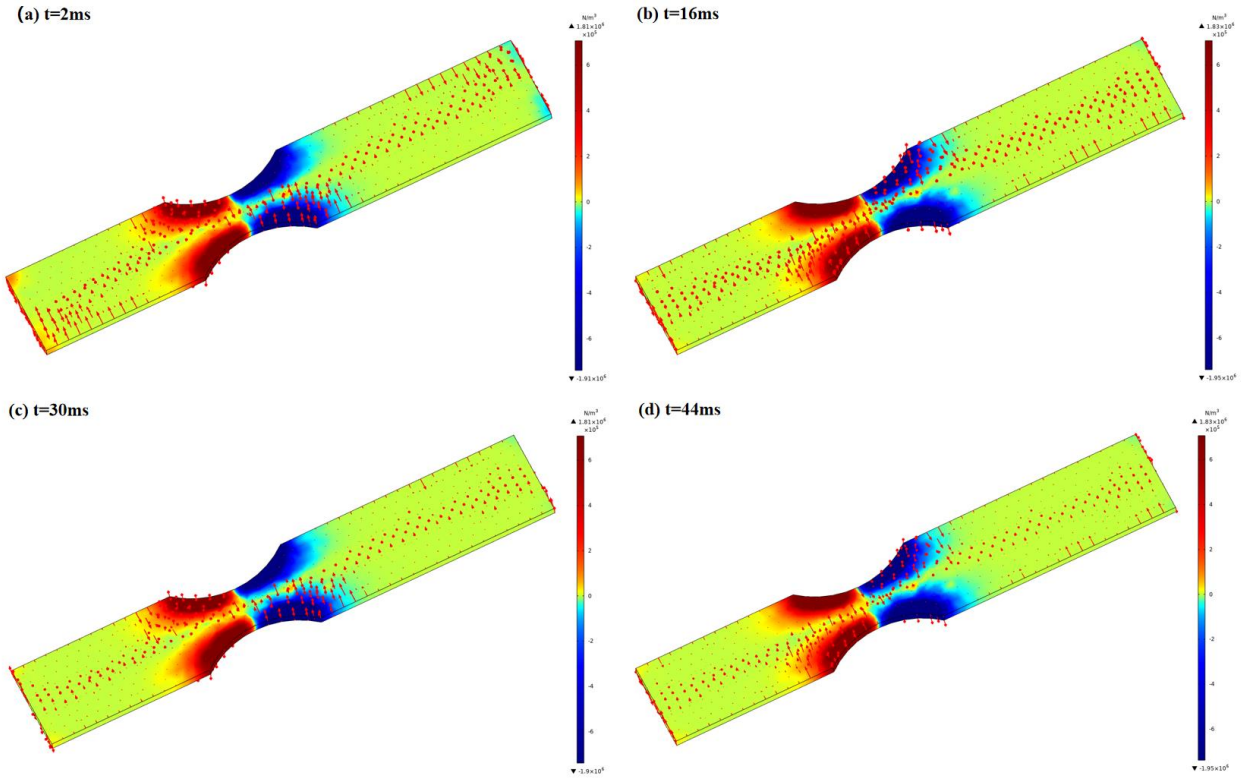

Fig. 23. Lorentz force distribution in a single CEMT period

3.4.4 COMSOL simulation model verification

Through simulation, we obtained the electromagnetic field distribution, temperature distribution and stress-strain variation trend of the sample in the CEMT process. In order to verify the reliability of the simulation results, we compared the temperature calculation and electromagnetic field acquisition results with the simulation results, so as to ensure the accuracy of the simulation model.

Li et al.[31, 32] found that the compressive residual stress on the surface of Ti2AlNb EBW joint is increased, this is due to the Joule heating effect during EMCT. The temperature increase of the sample by the Joule heating effect is estimated by the following equation:

$$\Delta T = \frac{\rho \int i^2 dt}{C_P d} \tag{6}$$

In the formula, i is the current density of the material, Cp is the specific heat capacity, ρ is the resistivity and d is the density of the material. Therefore, the Joule heating effect is mainly affected by the density of pulse current.

As can be seen from Table 4: Cp=605 (J/Kg·K), ρ =1.71×10-6(Ω·m), d=4.48(g/cm^3), $\int i^2 dt$=53.07A/mm^2, so ΔT =106.62K, consistent with the simulated temperature rise of 110K.

A. Babutskyi et al.[46] found that the samples also experienced a pulsed magnetic field as an integral side-effect of the current passing through the current-carrying sample. The magnitude of this field within the current-carrying sample was a function of the current (I) passing through the sample and the radial distance (r) across the central axis of the sample according to formula 7:

$$B = \mu_0 lr/(2\pi R^2) \tag{7}$$

Where μ_0 is a constant (i.e., the vacuum permeability) and R is the sample radius. Therefore, the magnetic field inside the sample was distributed proportional to r and varied with the current.

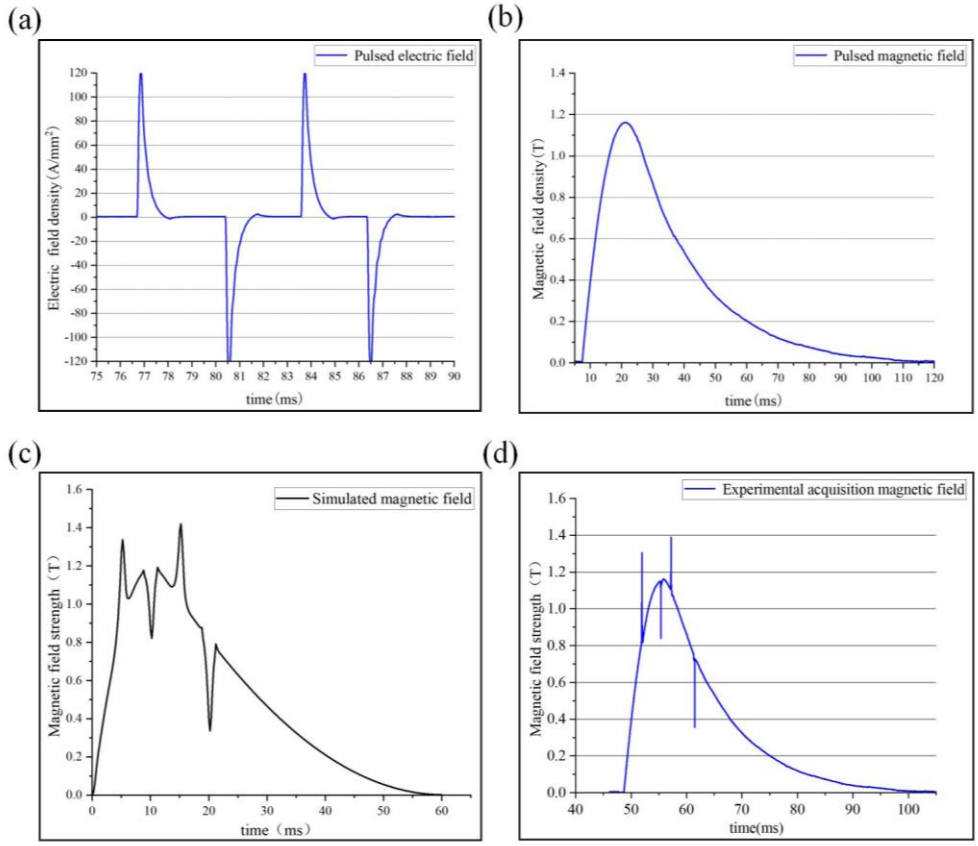

Fig. 24. (a) Pulsed electric field input model (b) Pulsed magnetic field input model (c) Coupling magnetic field simulation output model (d) Experimental output model of coupled magnetic field

As shown in Fig. 24, under the input conditions of pulsed electric field and magnetic field, the coupled magnetic field simulation results in the central region of the sample were compared with the experimental collection results of the coupled magnetic field, and it was found that under the simulation model, the coupling magnetic field output by the simulation was consistent with the

coupling magnetic field collected by the experiment.

By comparing the temperature rise formula calculation and the collected data of the coupled magnetic field with the simulation results, the reliability of the COMSOL simulation model in this study is verified, and the simulation results of this model have certain guiding significance for the experimental process.

4. Discussion

4.1 Mechanism of residual stress regulation during CEMT

In CEMT process, the current flowing through the sample will produce thermal effect, and the sample will produce instantaneous temperature rise. The temperature change in CEMT process can be expressed as formula 6.

The relation between strain and temperature in CEMT process can be expressed by formula 8.

$$\varepsilon = \alpha_t \Delta T \tag{8}$$

The stress-strain relationship of the material is formula 9.

$$\sigma = E_t \varepsilon \tag{9}$$

Et is the elastic modulus of the material at time *t*. Combining formula 6, formula 8 and formula 9, a numerical model of thermal stress and current density is established in this paper, as shown in formula 10:

$$\sigma = \frac{E_t \alpha_t \int_0^t \rho j^2(t) dt}{C_p d} \tag{10}$$

In CEMT process, the current flowing through the sample will produce thermal effect, and the sample will produce instantaneous temperature rise. The volume force form of charged particle *q* subjected to Lorentz force in electromagnetic field can be expressed by Eq. 11.

$$f = p \cdot E + J \times B \tag{11}$$

where *p* is the charge density and *J* is the current density. Since the order of magnitude of the charge density *p* is small, the Lorentz force is mainly the vector product of the current density *J* and the magnetic flux density *B*, and its direction is affected by the angle θ between the electric field and the magnetic field, which can be expressed by Eq. 12.

$$f = J \times B = \|J\| \cdot \|B\| \cdot \sin\theta \tag{12}$$

The stress-strain state of the electromagnetic coupling process is accumulated over time. Therefore, five points are set in the geometric model according to Fig. 3 to read the stress change state of the electromagnetic coupling process cycle, as shown in Figs. 25 and 26. Among them, points 2,4 and 5 are the stress changes in the length direction, and points 1,2 and 3 are the stress changes in the width direction. As shown in Fig. 17, in the direction of length, the current density of the sample is constantly changing, while the direction of current density is always parallel to the direction of magnetic field. It can be seen from equations 9 and 11 that the thermal stress in the direction of length plays a major regulating role, and it can be seen that the higher the current density, the better the regulating effect, In the width direction, the current density of the sample is unchanged, while the current density direction intersects with the magnetic field direction. Therefore, it can be seen from equation 12 that the Lorentz force in the width direction plays a major regulating role, and it can be seen that the higher the magnetic field intensity, the better the regulating effect. The stress in the length direction shows a gradual increasing trend as shown in Fig 25, which is caused by the decrease of the increase of the current density. The average stress is −72.9 MPa. The positions of points 1,2 and 3 are located at the beginning of the variable cross section, and there is an angle between the current direction and the magnetic field direction. Therefore, the force of the electromagnetic field gradually increases, and the stress across the width also shows an increasing trend, with an average stress of 6.8 MPa.

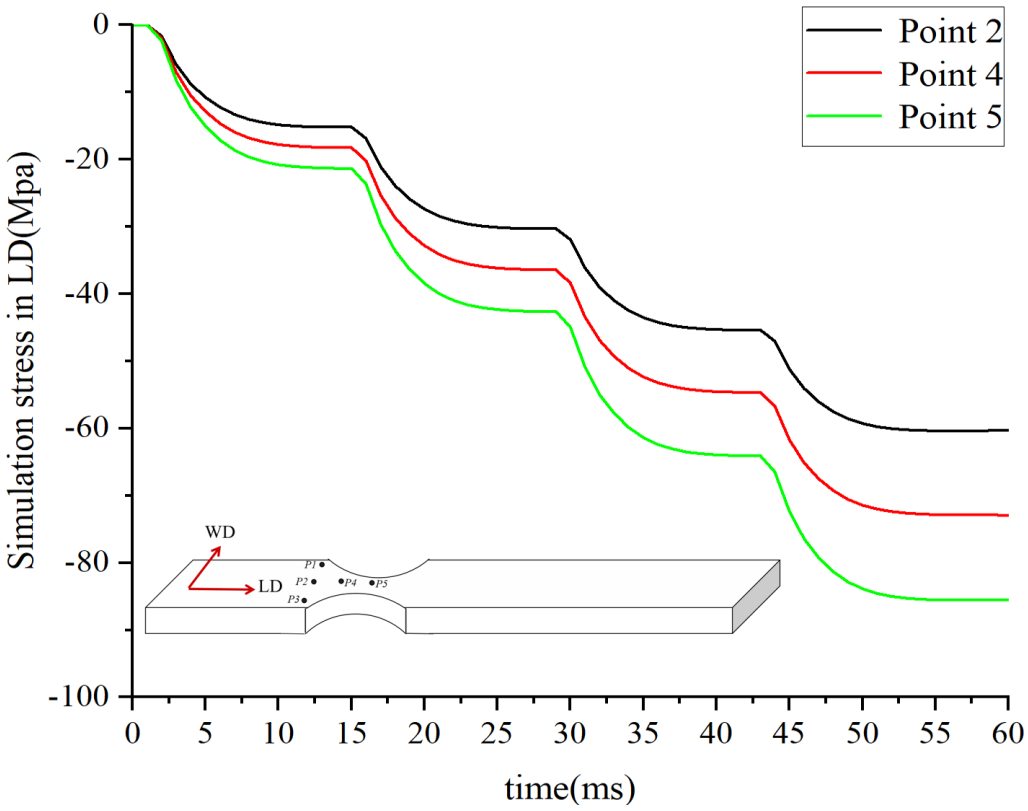

Fig. 25. Simulation stress in the length direction

The stress in the electromagnetic coupling process is non-linearly superimposed with the residual stress of the material. When the local stress of the material exceeds its yield limit, the material will undergo micro-plastic strain, and stress relaxation occurs at this time. During the CEMT process, the total strain ε_{tot} remains constant because there is no new deformation in the work-piece. The total strain ε_{tot} is composed of elastic strain ε_e, plastic strain ε_{pl}, and creep strain ε_c. Their relationship can be expressed as[47, 48]:

$$\varepsilon_{tot} = \varepsilon_e + \varepsilon_{pl} + \varepsilon_c = (\varepsilon_e + \Delta\varepsilon_e) + (\varepsilon_{pl} + \Delta\varepsilon_{pl}) + (\varepsilon_c + \Delta\varepsilon_c) \tag{13}$$

During the electromagnetic coupling process of the sample, the total strain (ε_{tot}) remains unchanged. According to the electro-plastic theory[29], the electromagnetic field generates a large amount of microplastic strain inside the material through energy transfer and accumulation, as shown in Fig 19, it is found that the plastic strain (ε_{pl}) on the surface of the sample increase under the action of thermal stress and Lorentz force, therefore, which improves the sample 's plasticity[49, 50]. Through microscopic analysis, it is found that the dislocation of the sample moves inward along the slip system under the action of the electromagnetic field.

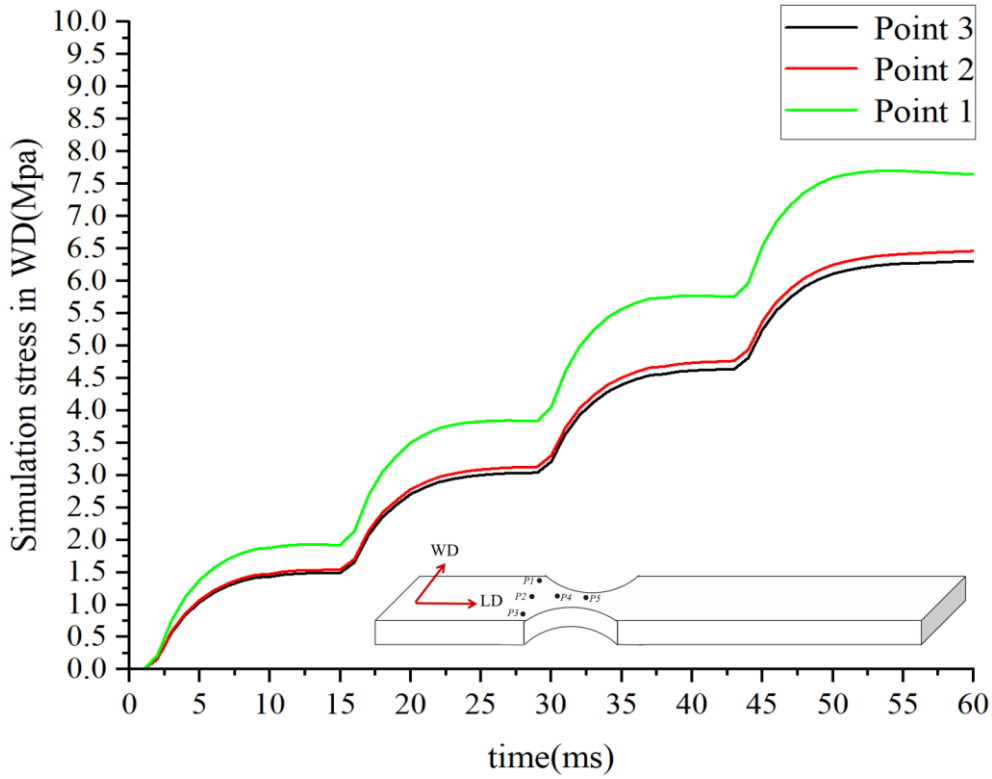

Fig. 26. Simulation stress in the width direction

The results in an increase in dislocation creep (ε_c)[51], which means that the plastic strain increment ($\Delta\varepsilon_{pl}$) and the creep strain increment ($\Delta\varepsilon_c$) are both positive. Because the total value is constant, the elastic strain increment ($\Delta\varepsilon_e$) is negative. The essence of the residual stress of the material is the storage of elastic strain energy. The negative elastic strain increment means that the residual stress increment is negative, that is, the residual compressive stress increases.

4.2 Mechanism of fatigue performance improvement after CEMT

Fatigue testing refers to the periodic loading and unloading process of the specimen under certain alternating load conditions. The residual stress (σ_{rs}) on the surface of the material, the thermal stress (σ_{ts}) and Lorentz force (σ_{lf}) introduced by CEMT will offset part of the external load (σ_{el}) applied by the fatigue test. The external load under the influence of residual stress, thermal stress and the Lorentz force can be expressed as:

$$\sigma_F = \sigma_{el} - \sigma_{rs} - \sigma_{ts} - \sigma_{lf} = \sigma_{el} - \sigma'_{rs} \tag{14}$$

Where σ_{rs} is the residual stress before CEMT and σ'_{rs} is the residual stress after CEMT. The Basquin's formula can be used to predict fatigue behavior in cycle fatigue tests, representing in the following form[52]:

$$\sigma_F = AN_f^b \tag{15}$$

Where σ_F is the stress amplitude, N_f is number of cycles to failure, A is the fatigue strength coefficient and b is the Basquin exponent. The stress distribution during the fatigue test of the specimen is shown in Fig. 27, and Eq. 15 can be expressed as:

$$\sigma_F = \sigma_{el} - \sigma_{rs} = AN_f^b \tag{16}$$

$$\sigma'_F = \sigma_{el} - \sigma'_{rs} = A\ (N'_f)^b \tag{17}$$

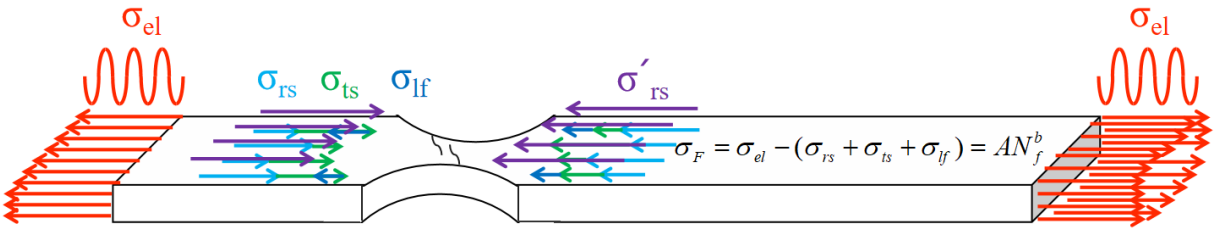

Fig. 27. Stress distribution in the fatigue test process

The parameter b in formulas 16 and 17 is negative, which means that the number of fatigue cycles is negatively correlated with the equivalent applied load (σ_F). When the equivalent applied load is smaller, the number of fatigue cycles of the sample is larger, and the fatigue performance of the sample is better. Through the above analysis, it can be seen that CEMT can induce creep strain by introducing plastic strain and promoting dislocation slip and proliferation. Plastic strain and creep strain will improve elastic strain, thereby regulating the sample's residual stress. The specific form is that the sample's residual compressive stress increases. Therefore, the equivalent applied load after CEMT is less than that before CEMT, so that the fatigue performance of the sample after CEMT is improved.

5. Conclusions

The present work experimentally studied residual regulation, dislocation movement and fatigue property strengthening in different TC11 titanium alloy specimens under pulsed electromagnetic treatment. The conclusions can be drawn as follows:

(1) CEMT can effectively increase the residual compressive stress in the length direction of TC11 titanium alloy specimens by 5.9 % to 63.7 %, and the residual compressive stress in the width direction by 6.1 % to 117.4 %. Under the optimal processing parameters (1.5 T, 120 A/mm^2), the residual compressive stress in the length direction and width direction increased by 63.7 % and 56.0 %, the

tensile strength remained unchanged, the elongation after fracture increased by 11.4 %, and the fatigue performance increased by 39.9%. The CEMT parameters have a certain reference value for further research.

(2) The CEMT process regulates the residual compressive stress by adjusting the elastic strain. The electric field introduces thermal stress, thereby introducing plastic strain. The magnetic field introduces a Lorentz force. The Lorentz force with periodic changes in size and direction promotes the movement and diffusion of dislocations, so that uniform microplastic strain and creep strain occur inside the material. The total strain of the CEMT process does not change. The increase of plastic strain and creep strain means the decrease of elastic strain, so the residual compressive stress increases.

(3) The Basquin's formula shows that the equivalent load applied by the material is negatively correlated with the number of fatigue cycles. When the residual compressive stress is larger, the equivalent load is smaller, the number of fatigue cycles of the sample is larger, so the fatigue performance is better. Through simulation and residual stress testing, it can be found that CEMT can regulate the residual stress field on the surface of the specimen through a thermal stress field and Lorentz force field, so as to improve the fatigue performance of the TC11 specimens.

Data availability

The raw/processed data required to reproduce these findings cannot be shared at this time due to technical or time limitations.

Authorship contribution statement

Hongfei Sun: Methodology, Data curation, Writing original draft, Software.

Liang Zhang: Formal analysis, Data curation.

Yuan Wang: Software, Validation.

Yi Qin: Conceptualization, Validation.

Zhiqiang Xie: Project administration, Validation.

Lila Ashi: Investigation, Data curation.

Ning Xu: Software, Data curation.

Kunlan Huang: Validation, Writing-review & editing, Funding acquisition.

Jie Wang: Conceptualization, Project administration.

Jigang Huang: Project administration, Validation.

Declaration of competing interest

The authors declare that they have no known competing financial interests or personal relationships that could have appeared to influence the work reported in this paper.

Acknowledgment

The authors wish to acknowledge the financial support by the National Nature Science Foundation of China (grant No. 52305398), Sichuan science and technology program (No. 2021ZDZX0001) and the AVIC Independent Innovation Special Fund Project (No. ZZCX-2022-036).

References:

[1] Pushp P, Dasharath SM, Arati C. Classification and applications of titanium and its alloys. Materials Today: Proceedings 2022;54:537-542.

[2] Abd-Elaziem W, Darwish MA, Hamada A, Daoush WM. Titanium-Based alloys and composites for orthopedic implants Applications: A comprehensive review. MATER DESIGN 2024;241:112850.

[3] Hartman AD, Gerdemann SJ, Hansen JS, Albany Research Center ARC AO. Producing lower-cost titanium for automotive applications. JOM (1989) 1998;50(9):16-19.

[4] Chowdhury TS, Mohsin FT, Tonni MM, Mita MNH, Ehsan MM. A critical review on gas turbine cooling performance and failure analysis of turbine blades. International Journal of Thermofluids 2023;18:100329.

[5] Singh HP, Rawat A, Manral AR, Kumar P. Computational analysis of a gas turbine blade with different materials. Materials Today: Proceedings 2021;44:63-69.

[6] Pomeroy MJ. Coatings for gas turbine materials and long term stability issues. MATER DESIGN 2005;26(3):223-231.

[7] Gurrappa I. An oxidation model for predicting the life of titanium alloy components in gas turbine engines. J ALLOY COMPD 2005;389(1-2):190-197.

[8] Mourad AI, Almomani A, Ahmad Sheikh I, Elsheikh AH. Failure analysis of gas and wind turbine blades: A review. ENG FAIL ANAL 2023;146:107107.

[9] Azevedo CRF, Sinátora A. Erosion-fatigue of steam turbine blades. ENG FAIL ANAL 2009;16(7):2290-2303.

[10] Poursaeidi E, Aieneravaie M, Mohammadi MR. Failure analysis of a second stage blade in a gas turbine engine. ENG FAIL ANAL 2008;15(8):1111-1129.

[11] Sivaprasad S, Narasaiah N, Das SK, Das G, Tarafder S, Gupta KK, Ghosh RN. Investigation on the failure of air compressor. ENG FAIL ANAL 2010;17(1):150-157.

[12] Poursaeidi E, Salavatian M. Failure analysis of generator rotor fan blades. ENG FAIL ANAL 2007;14(5):851-860.

[13] Pokorný P, Dlhý P, Poduška J, Fajkoš R, Vojtek T, Náhlík L, Grasso M, Hutař P. Influence of heat treatment-induced residual stress on residual fatigue life of railway axles. THEOR APPL FRACT MEC 2020;109:102732.

[14] Hirohata M, Chang K, Suzuki T, Konishi H. Local heating for reducing residual stress and fatigue-performance improvement of welded joints. J CONSTR STEEL RES 2024;215:108544.

[15] Giri Saputro M, Muhayat N, Triyono. Residual stress effect on fatigue behavior of steel welded: A review. Materials today : proceedings 2023.

[16] Shu S, Shen Y, Cheng Z, Xiong W, He Z, Song S, Liu W. Laser shock peening regulating residual stress for fatigue life extension of 30CrMnSiNi2A high-strength steel. Optics & Laser Technology 2024;169:110094.

[17] Chiocca A, Frendo F, Bertini L. Residual stresses influence on the fatigue strength of structural components. Procedia Structural Integrity 2022;38:447-456.

[18] Vaara J, Kunnari A, Frondelius T. Literature review of fatigue assessment methods in residual stressed state. ENG FAIL ANAL 2020;110:104379.

[19] Ramakokovhu U, Desai D, Snedden G, Jamiru T. Significance of residual stresses in fatigue life prediction of micro gas turbine blades. ENG FAIL ANAL 2021;120:105092.

[20] Perić M, Tonković Z, Rodić A, Surjak M, Garašić I, Boras I, Švaić S. Numerical analysis and experimental investigation of welding residual stresses and distortions in a T-joint fillet weld. MATER DESIGN 2014;53:1052-1063.

[21] Areitioaurtena M, Segurajauregi U, Fisk M, Cabello MJ, Ukar E. Influence of induction hardening residual stresses on rolling contact fatigue lifetime. INT J FATIGUE 2022;159:106781.

[22] CHEN G, XIU Z, YANG W, JIANG L, WU G. Effect of thermal-cooling cycle treatment on thermal expansion behavior of particulate reinforced aluminum matrix composites. T NONFERR METAL SOC 2010;20(11):2143-2147.

[23] Soyama H, Chighizola CR, Hill MR. Effect of compressive residual stress introduced by cavitation peening and shot peening on the improvement of fatigue strength of stainless steel. J MATER PROCESS TECH 2021;288:116877.

[24] Qin Z, Li B, Chen R, Zhang H, Xue H, Yao C, Tan L. Effect of shot peening on high cycle and very high cycle fatigue properties of Ni-based superalloys. INT J FATIGUE 2023;168:107429.

[25] Zhan K, Jiang CH, Ji V. Uniformity of residual stress distribution on the surface of S30432 austenitic stainless steel by different shot peening processes. MATER LETT 2013;99:61-64.

[26] Zhong F, Wang J, Zhang Q, Huang J, Wang W, Xu J, Huang K, Qin Y. Residual stress reductions of carbide cutting tools through applying pulsed magnetic field and coupled electromagnetic field mechanism analysis and comparison study. INT J ADV MANUF TECH 2022;121(7-8):4757-4775.

[27] Cai Z, Huang X. Residual stress reduction by combined treatment of pulsed magnetic field and pulsed current. Materials Science and Engineering: A 2011;528(19-20):6287-6292.

[28] Ashi L, Xie Z, Sun H, Wang J, Huang K. Effect of electromagnetic coupling treatment on the residual stress relief and mechanical properties of 7050 aluminum alloy. J MATER SCI 2023;58(29):12097-12117.

[29] Bo Z, Dongyan C, Hongfei S, Juan D, Jie W, Kunlan H. Improvement in plasticity of Al-Cu-Mg alloy by electromagnetic coupling treatment. MATEC web of conferences 2024;401:4007.

[30] Zeng B, Yan X, Xie Z, Liu J, Wang J, Huang K, Yang Y. Plastic Deformation Mechanism of the Ti6Al4V Micro-gear Formed Under an Electrical Field. INT J PR ENG MAN-GT 2024;11(1):107-122.

[31] Li Q, Wang X, Qin Y, Huang K, Wang J. Improvement of the fatigue life of an electron-beam welded Ti2AlNb joint subjected to an electromagnetic coupling treatment. Materials Science and Engineering: A 2024;909:146848.

[32] Zhang Q, Wang X, Qin Y, He G, Zhang S, Huang K, Wang J. Improving thermal conductivity of a nickel-based alloy through advanced electromagnetic coupling treatment. Journal of materials research and technology 2022;21:4708-4723.

[33] Yuan M, Wang J, Wang L, Zhong F, Huang K, Tian Y. Electromagnetic coupling field strengthening of WC-TiC-Co cermet tools. CERAM INT 2021;47(3):3747-3759.

[34] Zhang Q, Huang K, Wang J, Wang L, Yuan M, Tian Y, Ouyang L. Effect of pulse electromagnetic coupling treatment on thermal conductivity of WC-8Co cemented carbide. CERAM INT 2021;47(16):22683-22692.

[35] Song Y, Wang Z, Yu Y, Wu W, Wang Z, Lu J, Sun Q, Xie L, Hua L. Fatigue life improvement of TC11 titanium alloy by novel electroshock treatment. MATER DESIGN 2022;221:110902.

[36] Ren X, Wang Z, An R. A promising approach to enhance fatigue life of TC11 titanium alloy: Low dislocation density and surface grain refinement induced by electropulsing. J MATER SCI TECHNOL 2025;204:60-70.

[37] Enhanced fretting fatigue strength of TC11 titanium alloy using laser-assisted ultrasonic surface rolling process.

[38] Xie L, Ren S, Yin F, Wang F, Qian D, Song Y, Hua L, Wang L, Zhang L, Lu W. Effects of three stress levels on the fatigue properties and fracture mechanisms of an in-situ synthesized TiB/Ti-6Al-4V titanium matrix composite. MATER CHARACT 2023;195:112511.

[39] Fujiyama K, Mori K, Kaneko D, Kimachi H, Saito T, Ishii R, Hino T. Creep damage assessment of 10Cr-1Mo-1W-VNbN steel forging through EBSD observation. INT J PRES VES PIP 2009;86(9):570-577.

[40] Song X, Wang F, Qian D, Hua L. Tailoring the residual stress and mechanical properties by electroshocking treatment in cold rolled M50 steel. Materials science & engineering. A, Structural materials : properties, microstructure and processing 2020;780:139171.

[41] Liu C, Xie L, Qian D, Hua L, Wang L, Zhang L. Microstructure evolution and mechanical property response of TC11 titanium alloy under electroshock treatment. MATER DESIGN 2021;198:109322.

[42] Sun Q, Hua L. Micro texture of titanium alloys excited nonlinearly by electromagnetic pulse. SCRIPTA MATER 2021;200:113828.

[43] Chai Z, Wang WY, Ren Y, Wang X, Zhang Y, Sun F, Hao F, Li J. Hot deformation behavior and microstructure evolution of TC11 dual-phase titanium alloy. Materials Science and Engineering: A 2024;898:146331.

[44] Kamaya M, Wilkinson AJ, Titchmarsh JM. Measurement of plastic strain of polycrystalline material by electron backscatter diffraction. NUCL ENG DES 2005;235(6):713-725.

[45] Ananthakrishna G. Current theoretical approaches to collective behavior of dislocations. Physics Reports 2007;440(4-6):113-259.

[46] Babutskyi A, Mohin M, Chrysanthou A, Xu Y, Lewis A. Effect of electropulsing on the fatigue resistance of aluminium alloy 2014-T6. Materials science & engineering. A, Structural materials : properties, microstructure and processing 2020;772:138679.

[47] Xiong H, Zhou Y, Yang P, Kong C, Yu H. Effects of cryorolling, room temperature rolling and aging treatment on mechanical and corrosion properties of 7050 aluminum alloy. Materials Science and Engineering: A 2022;853:143764.

[48] Rahimi S, King M, Dumont C. Stress relaxation behaviour in IN718 nickel based superalloy during ageing heat treatments. Materials Science and Engineering: A 2017;708:563-573.

[49] Rogachev SO, Zavodov AV, Naumova EA, Chernenok TV, Lukina EA, Zadorozhnyy MY. Improvement of strength – ductility balance of Al – Ca – Mn – Fe alloy by severe plastic deformation. MATER LETT 2023; 49: 34797.

[50] Jeong CU, Choi J, Park H, Han JH. Effects of pre-deformation mode on non-homogeneity of plastic deformation and mechanical properties in Al – Cu – Mg – Ag alloy. Journal of materials research and technology 2024; 1: 376-2387.

[51] Peng Z, Zou J, Wang X. Microstructural characterization of dislocation movement during creep in powder metallurgy FGH96 superalloy. Materials Today Communications 2020;25:101361.

[52] Cao S, Zhang H, Hu J, Li C, Li B. Fatigue life prediction model for shot-peened laser powder bed fused 304L steel considering residual stress relaxation and defect distribution. ENG FAIL ANAL 2024;162:108423.